Lappeenranta University of Technology
School of Engineering Science
Computational Engineering and Technical Physics

Master's Thesis

Kristina Bespalova

EXPERIMENTAL MEASUREMENT OF YOUNG'S MODULUS OF GALLIUM PHOSPHIDE NANOWIRES BY ATOMIC FORCE MICROSCOPY

Examiners: Professor Erkki Lähderanta

M.Sc Pavel Geydt

ABSTRACT

Lappeenranta University of Technology
School of Engineering Science
Computational Engineering and Technical Physics

Kristina Bespalova

Experimental measurement of Young's modulus of Gallium Phosphide Nanowires by Atomic Force Microscopy

Master's Thesis

2018

80 pages, 66 figures and 3 tables

Examiners: Professor Erkki Lähderanta
M.Sc Pavel Geydt

Keywords: gallium phosphide, nanowires, AFM, Euler-Bernoulli beam theory, mechanical properties, Young's modulus

Mechanical characteristics of tapered mixed composition (wurtzite and zincblende) Gallium Phosphide (GaP) nanowires (NWs) were investigated by Atomic Force Microscopy (AFM).

Experimental measurements and numerical modeling of experimental data for calculation of Young's modulus of free-standing (in single-clamped geometry) inclined GaP NWs on p-Si (111) substrate were obtained by Quantitative Nanomechanical Mode of AFM. Calculations were performed applying Euler-Bernoulli beam theory.

Acknowledgments

I want to thank all the people who supported my decision to continue my studies after obtaining a bachelor's degree, and then take part in the Double Degree Program.

First of all, I want to thank Professor Erkki Lähderanta for giving me the opportunity to study at Lappeenranta University of Technology. Without him, this work would have been impossible.

I would like to thank my supervisor Pavel Geydt for all the time that he spent teaching me, giving advices on how to improve my thesis and directing me in experimental work.

I am grateful to Vladislav Khayrudinov from Aalto University for samples of nanowires that were grown by him and subsequently investigated in this work, and to Prokhor Alekseev and Mikhail Dunaevskiy from Ioffe Institute for advices they gave to me.

I am also grateful to Professor Vyacheslav Alekseevich Moshnikov, to Yuliya Mikhailovna Spivak and to Alexandra Nikolaevna Krivosheeva from department of Micro- and Nanoelectronics Technology in St. Petersburg State Electrotechnical University for their advices and support.

Finally, I want to thank all my friends and family for encouragement, willingness to help and patience during the time of writing this paper. Individual gratitude to wonderful Pavel Somov, who was ready to help me at every stage of the work.

Lappeenranta, May 2018

Kristina Bespalova

Abbreviations

AFM	Atomic Force Microscopy/Atomic Force Microscope
CVD	Chemical Vapor Deposition
FB	Feedback
FIB	Focused Ion Beam
LED	Light Emitting Diode
MOVPE	Metalorganic Vapor Phase Epitaxy
NPs	Nanoparticles
NW	Nanowire
QNM	Quantitative Nanomechanical Properties Mapping
SEM	Scanning Electron Microscopy
SPM	Scanning Probe Microscopy
VSL	Vapor–Liquid–Solid

TABLE OF CONTENTS

ABSTRACT
ACKNOWLEDGMENTS
ABBREVIATIONS
1. INTRODUCTION **1**
1.1. Gallium phosphide crystals **1**
1.2. Applications of gallium phosphide nanowires **3**
1.3. Review of nanowires' fabrication methods **7**
1.3.1. Chemical vapor deposition **8**
1.3.2. Vapor-Liquid-Solid method **9**
1.3.3. Template synthesis **12**
2. METHODICAL PART **14**
2.1. Scanning Electron Microscopy **14**
2.2. Atomic Force Microscopy **17**
2.2.1. AFM cantilevers **21**
2.2.2. PeakForce QNM mode **24**
2.3. Euler-Bernoulli beam theory **25**
3. EXPERIMENTAL PART **31**
3.1. Technological parameters for GaP NWs **31**
3.2. Measurement procedure **34**
3.3. Experimental data processing **47**
4. RESULTS AND DISCUSSION **50**
4.1. Experimental results **50**
4.2. Analysis of experimental results **56**
4.3. Prospects for the experiment **57**
CONCLUSIONS **62**
SUMMARY **64**
REFERENCES **65**
APPENDIX I. LIST OF FIGURES

1. INTRODUCTION

Nanostructured gallium phosphide is a promising material for use in electronics [1-3], biology [4-7], photovoltaics [8], and also for the creation of renewable energy sources [9]. Due to the creation of nanostructures based on gallium phosphide, a number of problems can be solved without significant material costs. However, when going to nanoscale, some material properties tend to suffer changes. In particular, this is also true for the mechanical properties of nanostructures, such as flexibility coefficient [10] and Young's modulus [11-13]. According to the size of such structures it is crucial to use precise instruments, for example AFM.

Therefore, the motivation of this work was to investigate the mechanical properties of GaP NWs by AFM, namely Young's modulus. Since the experimental results on the evaluation of the Young's modulus for GaP NWs have not been obtained previously, the second interest was to highlight the features of working with namely GaP NWs and to develop methods that will further improve the AFM bending experiment.

1.1. Gallium Phosphide Crystals

The compounds of gallium with elements of the fifth group of the periodic table were firstly described more than 60 years ago by H. Welker and represented in 1956 in the work [14]. GaP is $A^{III}B^{V}$ type semiconductor with a indirect bandgap of 2.26 eV at room temperature and zincblende (face-centered cubic as shown at Figure 1, a) crystal structure with lattice constant a = 0.545 nm. Figure 1 presents different types of crystal lattices. Monocrystals of gallium phosphide have the greatest prospects for industrial production of different electronic components, due to a wide bandgap (in comparison with 1.14 eV for Si and 1.43 eV for GaAs at room temperature) [15].

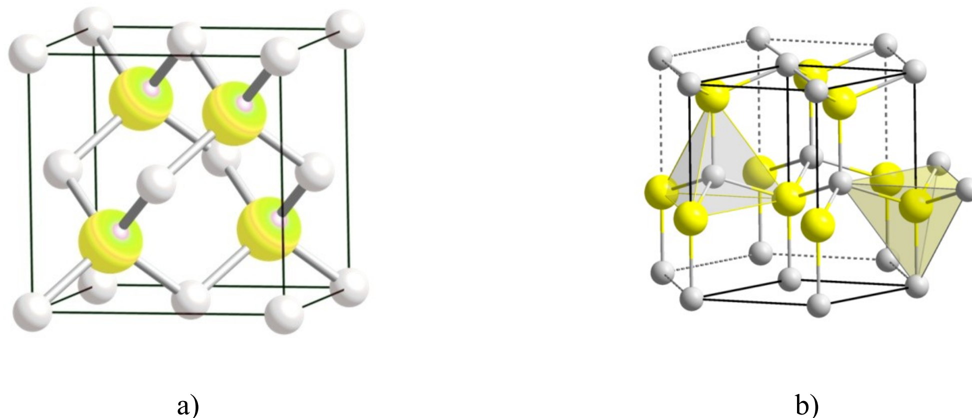

a) b)

Figure 1. Crystal structure: a) zincblende; b) wurtzite (white – P, yellow – Ga).

Gallium phosphide is resistant to the action of air oxygen up to ~ 700 ° C. It does not react with water, practically does not react with H_2SO_4 and hydrochloric acid. It slowly reacts with heating with nitric and hydrofluoric acids and decomposes by solutions of alkalis upon heating with release of PH_3.

In the form of a bulk material, GaP is obtained by fusing Ga with P under phosphorous vapor pressure. Gallium directly interacts with phosphorus vapor at high temperatures to form GaP phosphide. Along with a direct method of synthesis, many indirect methods have been proposed. For example, such as the action of hydrogen phosphorous at high temperatures on a metal or gallium oxide, or the action of phosphorus vapor in a mixture with hydrogen, on gallium oxide, phosphorus trichloride on gallium. To produce small monocrystals and GaP thin films, gas phase reactions are used, such as the interaction of phosphorus vapor with gallium oxide [16]:

$$3Ga_2O + 2P_4 \rightarrow 6GaP + P_2O_3 \quad \textbf{(1)}$$

Or in the interaction of phosphorus vapor with gallium monohalides:

$$6GaCl + P_4 \rightarrow 4GaP + 2GaCl_3 \quad \textbf{(2)}$$

Monocrystals are grown by Float Zone Technique or by Czochralski method from the B_2O_3 flux under Ar pressure [16]. Te, Se, S, Sn, Zn, Cd, and Ge impurities are used for doping of monocrystals and thin films of GaP. When the bulk material is formed by the Czochralski method, it forms orange crystals as demonstrated in Figure 2.

Figure 2. GaP Wafers grown by Czochralski extrusion taken from [17].

Since the 1960s GaP has been used to manufacture inexpensive LEDs. Gallium Phosphide is used also as material for optical instruments. The refractive index of GaP is 4.3;

3.45; 3.18 for wavelengths of 262 nm (ultraviolet radiation), 550 nm (green light) and 840 nm (near infrared), respectively, and is higher than in most optical materials, for example, the refractive index of diamond 2.4 [18].

1.2. Applications of Gallium Phosphide Nanowires

Nanomaterials are usually divided into four main types accordingly to dimensions of their structural elements: zero-dimensional (0D), one-dimensional (1D), two-dimensional (2D) and three-dimensional (3D). NWs refer to one-dimensional nanostructures, the size of which in one direction is typically much larger than the size of the other two, the latter being in the "nano" range (that is less than 100 nm) [19]. The dimension in one of the directions considerably exceeds (by more than an order of magnitude) the size in the other two directions, the particle can be considered to be cylindrical with a height considerably exceeding the diameter. Figure 3a, shows a SEM image of typical GaP NWs grown on a silicon substrate.

The main idea for all nanomaterials is to gain new physical and chemical properties in comparison with macro scale material. Let's consider what properties appear in nanostructures of GaP and the application for such materials.

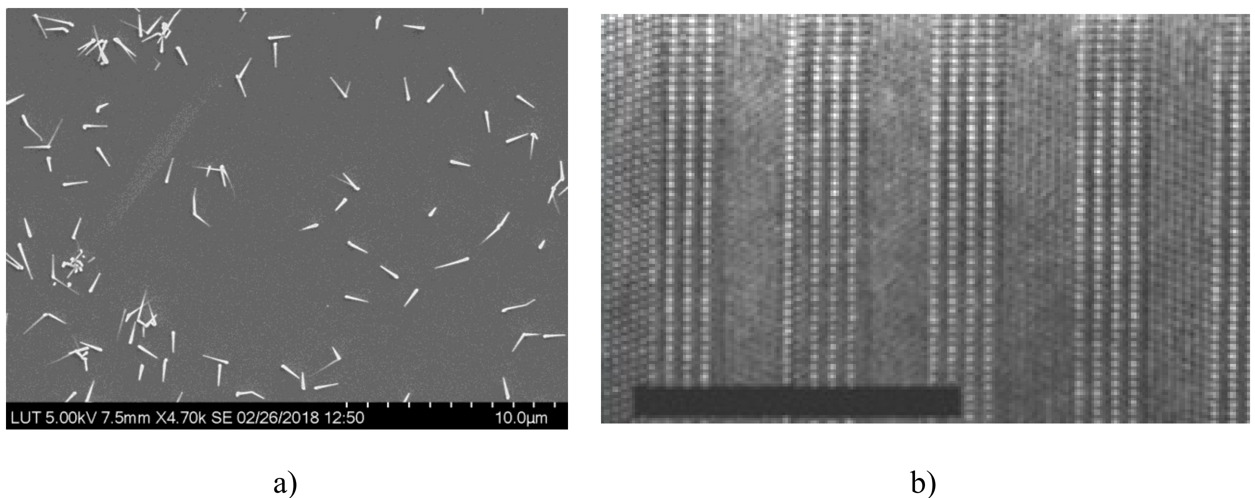

a) b)

Figure 3. a)SEM image of GaP NWs (white) located on a flat Si substrate (grey background), b) TEM image of NW showing mixed ZB/WZ phases, scale bar: 20 nm.[35].

Bulk gallium phosphide is an indirect-gap semiconductor from the $A^{III}B^{V}$ class, which typically crystallizes in a cubic structure of the zincblende type. However, when forming NWs from GaP, it is possible to obtain not only zincblende type crystal lattice, but also a wurtzite type, as shown in Figure 3b [20]. Such NWs, in turn, have unique properties that are absent in bulk gallium phosphide. For example, it is piezoelectric properties and luminescence due to direct bandgap, which emerges in GaP crystals at nanolevel [21].

In work [22] the possibility of using wurtzite GaP NWs for optoelectronic devices is considered. In this work, GaP NWs were obtained by the CVD method had a diameter of 20-80 nm with an average diameter of 40 nm and a length of few micrometers. Silicon was used as the substrate for lying NWs. The NWs in this geometry have shown broad and intense peaks at 364 cm^{-1} and 398 cm^{-1} confirmed from transverse optic and longitudinal optics phonons by Raman spectrometer. Photoluminescence (PL) spectra showed four intense and five sub- PL peaks in the range 2.05 – 2.35 eV. In the opinion of the authors, such wide range for emission arises as a consequence of the large presence of defects in the resulting structure, as well as due to inclusions of silicon from the substrate. Also, in [23], other research group investigated the photoluminescence of GaP NWs in similar geometry, and observed a sharp peak at 2.14 eV. In both cases, the authors explain the presence of a luminescence peak by a direct bandgap formed in GaP due to size effects. The broadening of the emission peak is presumably due to impurity atoms.

The authors of [8] investigated the possibility of using of gallium phosphide NWs for photovoltaic structures. Heterostructures based on GaP–ZnO core–shell NW when used as solar cells, can broaden its spectral sensitivity region toward shorter wavelengths, improve the photon absorption, and diminish light reflection. The type of conductivity, concentration and mobility of charge carriers in a field-effect transistor (FET) based on GaP NW is estimated in the paper [8]. A NW-based FET was obtained as follows: the NW was separated from the substrate and placed on Si / SiO_2 pads. To create an ohmic contact, an alloy with Au + 5% Zn was used. For contact at the gate - aluminum, deposited by magnetron sputtering was used. As a result of measuring electrical properties, it was found that NW FET exhibits p-type conductivity with hole concentration $p = 0.9–1.5\cdot10^{18}$ cm^{-3}, and hole mobility $\mu = 4.7-9$ $cm^2 V^{-1} s^{-1}$. These parameters at the moment are much inferior to the parameters of other materials widely used in photovoltaics, such as silicon. However, the authors believe that they can be significantly improved by varying the technological parameters of obtaining NWs. Figure 4 shows the I-V curve plotted in [8].

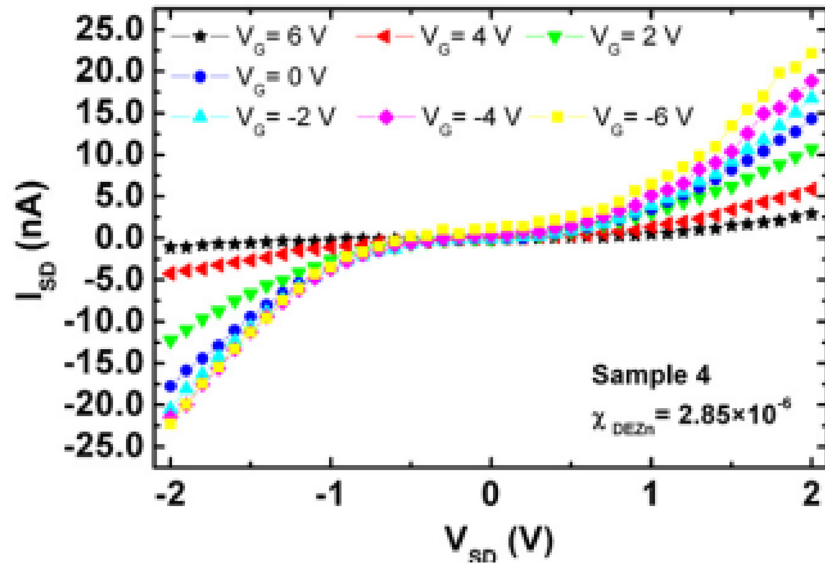

Figure 4. Nanowire FET source–drain current I_{SD} versus source–drain voltage V_{SD} characteristics measured at variable gate voltage V_G taken from [8].

NWs, being representatives of the class 1D materials, can be used as antennas [24], cavities for light [25-26], photodetectors [27], single photon sources [28], and lasing and emitting devices [29]. In [30], the high efficiency of using gallium phosphide NWs as antennas is noted in view of a high reflection index (about 3.4) of this material and bandgap in the visible at 548 nm wavelength.

However, NWs can be used not only in microelectronics, but also in biology, biomedicine, for fields of green chemistry and renewable energy. For example, in [4] it is noted that an array of ordered gallium phosphide NWs can be used as an elastic substrate for measuring cell forces. The method of measuring cell forces is based on measuring the force of deflection of NWs under the pressure of cell colonies grown on them. Using confocal microscopy, one can measure the position of each NW and then evaluate the dynamics of the deflection of NW under the pressure of different cell colonies.

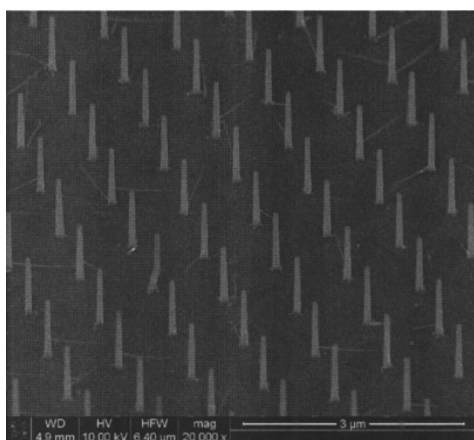

a)

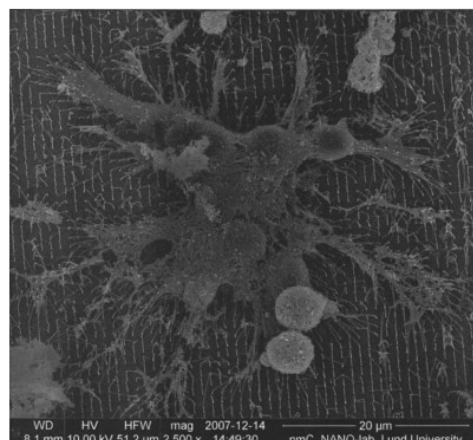

b)

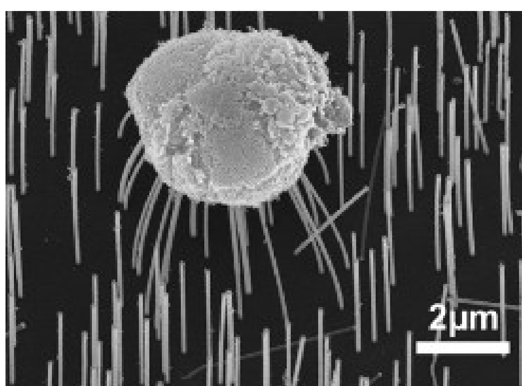

c)

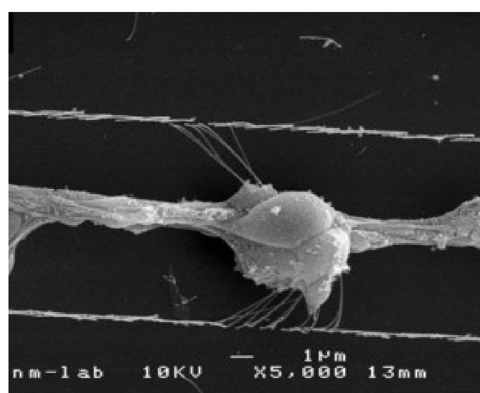

d)

Figure 5. SEM-images showing: a) ordered array of GaP NWs, b) nerve cells from dissociated dorsal root ganglia on a GaP NW array, c) retinal cells on GaP NWs, d) axons grow in the middle of two rows of NWs. The images are taken from [4-7].

The authors note: "These arrays seem very promising for applications in growth-cone force dynamics investigations, where the nerve fiber dimensions as well as the forces involved are very small" [4]. Also, the work [5] shows that nerve cells can successfully grow on arrays of GaP NWs as well as synaptophysin, retinal cells [6], axons [7]. Examples of the obtained structures are presented in Figure 5.

The authors of article [9] suggest to use arrays of NWs of gallium phosphide for the production of photoelectrochemical hydrogen from water and solar energy. This type of fuel is considered as a promising, clean and sustainable type of fuel of the future. Namely GaP NWs showed the highest efficiency in this direction due to the combination of a large absorptive capacity of sunlight, ideal band-edge positions for full water splitting, optimal bandgap, and chemical stability in aqueous solution. Also, photocathodes based on GaP have already been presented in the works [31-33].

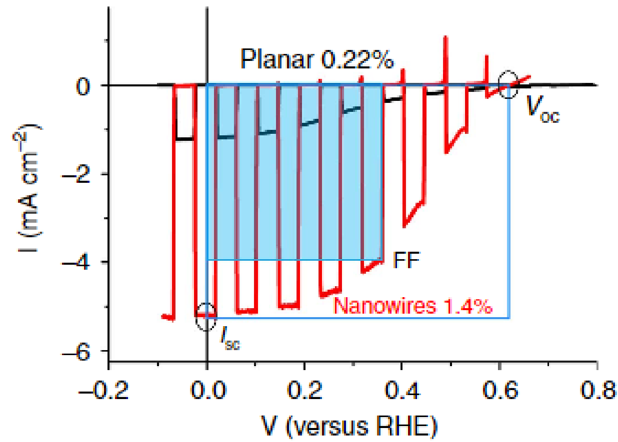

Figure 6. Linear sweep voltammograms for direct comparison of NW (red) and planar (black) samples with molybdenum sulphide catalyst, performed under chopped 100 mWcm^{-2} AM1.5 illumination, in aqueous solution pH 0 with $HClO_4$ as supporting electrolyte. Also showing open circuit potential (V_{OC}), short circuit current (I_{SC}) and fill factor ff (filled square/empty square) [9].

In all these works, the mechanical properties of NWs of gallium phosphide are involved. In calculations, Young's module of GaP NWs is engaged, it is assumed to be equal to 160 GaP. This value is correct for bulk material, however, according to the data of studies [10-13] Young's modulus is a dynamic value, which depends on the dimension of the crystal and suffers significant changes at nanoscale level. A more accurate value of the Young's modulus for this material will help to make more accurate calculations in all the above mentioned areas, respectively.

1.3. Review of Nanowires' fabrication methods

All methods of fabrication of semiconductor NWs can be divided into two main approaches: top-down and bottom-up [34-35]. In the first approach, to create NWs, on the top of bulk semiconductor wafer, combination of lithography, etching, doping and deposition methods are used. The advantage of this approach is that the NWs obtained in this way are located in a strictly defined sequence and occupy the necessary parts of the substrate. In addition, due to their similarity, such NWs easily integrate into any nanomechanical systems. However, this approach has its drawbacks, such as high production costs and limitations for NWs diameter, associated with the capabilities of photomasks for lithography. These shortcomings of the top-down approach pushed the scientists to find new ways of obtaining NWs to meet the demand for nanoscale structures. An alternative method for creating NWs is the bottom-up approach, which uses the methods of chemical synthesis and assembly of nanoelements from individual atoms or

molecules on a substrate. It is assumed [34], that the bottom-up approach has more potential and functionality for NWs fabrication than the top-down approach. In this chapter, bottom-up fabrication methods are discussed.

1.3.1 Chemical vapor deposition

CVD is a process, where gaseous react to form a solid coating on a heated substrate.

The formation of one-dimensional nanostructures in the CVD process occurs due to anisotropic growth by several mechanisms, for example [36]: different growth rates for different crystal faces. For example, in case of silicon, the growth rate of {111} faces is less than that of {110} faces or due to the presence of defects in certain directions of the crystal, for example, in the direction of the screw dislocation. Preferred accumulation or contamination by impurities of certain crystal faces.

The usual growth of crystals occurs according to the sequence of steps shown in Figure 7:

(1) The diffusion of growth particles from the vapor or liquid phase to the growth surface.

(2) Adsorption and desorption of growth particles on and from the growing surface.

(3) Diffusion over the surface of adsorbed growth particles. During diffusion along the surface, the adsorbed particles can either be inserted in the growth position, which leads to crystal growth, or escapes from the surface back to the vapor or liquid phase.

(4) The growth of the surface due to the irreversible introduction of adsorbed growth particles into the crystal structure. With sufficient supersaturation or high concentration of growth particles, this process will be a step limiting the growth rate and will determine the growth rate of the crystal.

(5) If by-products are formed on the surface during growth, they will be desorbed from the growth surface, making vacant place, so the growth particles will be adsorbed to the surface and the crystal growth process will continue.

(6) The by-products diffuse from the surface to release growth positions for further growth of the crystal.

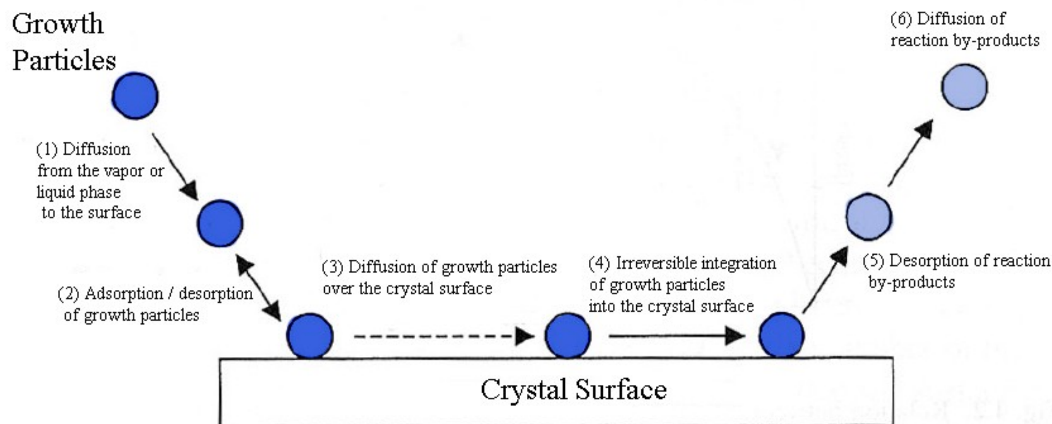

Figure 7. Schematic representation of the phased growth of a crystal occurring during a heterogeneous reaction taken from [36].

Different faces of the crystal have different surface energies. Different faces in a particular crystal are characterized by different atomic densities, in addition, atoms on different faces have a different number of broken connections, resulting in different surface energies. Such a difference in the energy of surfaces or the number of broken chemical bonds leads to different mechanisms and growth rates. For a flat surface, the classical theory of such growth was developed by Kossel, Stranski and Volmer [37]. They found that the surface of the crystal at the atomic level is not smooth or uniform, and it is the inhomogeneities responsible for crystal growth. Thus, crystal growth in this mechanism will occur due to the presence of defects on the surface of the crystal, for example, such as screw dislocations.

1.3.2. Vapor-Liquid-Solid method

When crystals grow according to the mechanism of the Vapor-Liquid-Solid (VLS), an additional substance (often called a catalyst) is deliberately introduced into the system. The catalyst promotes crystal growth in one direction and restricts growth in other directions to give the crystal a certain orientation. During growth, the catalyst forms a liquid phase consisting of the material of the catalyst or the product of its interaction with the material of the growing crystal. The liquid assembles into a droplet and this droplet serves as a trap for particles of growing material. Gradually the droplet becomes enriched with particles of a growing substance and they settle on the growth surface (substrate), which leads to the growth of crystals in one direction. The theory of growth by the mechanism of the VLS was proposed more than 50 years ago in explaining the experimental results and observations obtained with the growth of silicon NWs in work [38]. These phenomena could not be explained within the framework of the evaporation-condensation theory as in CVD. These phenomena include [36]:

1. Absence of screw dislocations or other defects along the direction of growth;

2. The growth direction [111] is the slowest in comparison with other directions with low indices, for example, [110] in silicon;

3. Necessary presence of impurities;

4. The presence of thickenings on the vertices (‘heads’) of whiskers.

The general requirements for the growth of crystals by the mechanism of VSL are as follows: firstly, the catalyst should form a liquid solution at the deposition temperature of the growing crystal. The catalyst distribution coefficient should be less than one at the deposition temperature. The equilibrium pressure of the catalyst vapor over the liquid droplet must be low. Although the evaporation of the catalyst does not change the composition of the saturated solution of the liquid, but it reduces the total volume of the droplet. If the additional amount of catalyst does not enter the drop, its volume decreases. Thus, the diameter of the NW will decrease and the growth of the crystal will stop when the catalyst evaporates completely. The catalyst must be chemically inert. It should not react, for example, with the byproducts that form in the growth chamber. Secondly, a very important role is played by the surface energy. Wetting affects the diameter of the growing NW. For a given volume of a catalyst droplet, a small contact angle leads to a large growth area, and hence to the growth of NWs of large diameter. Finally, with the growth of NWs of complex composition, one of the constituents may act as a catalyst. For controlled growth in one direction, the solid-liquid interface must be well crystallographically determined. In this case, one of the simplest methods is the use of a single crystal substrate with the desired crystal orientation.

The process of NW growth by the mechanism of the VLS can be described, as shown schematically in Figure 8. First, metal nanoparticles (Au, Ag, Cu, Al, Au or their alloys) are employed on the substrate [39]. Since due to nanoscale effects, metal nanoparticles have a lower melting point than bulk metals, this makes the VLC process possible [40]. Further, after increasing the temperature, nanoparticles and a substrate form a liquid metal–semiconductor eutectic alloy. Then, the particles of the growing material evaporate, diffuse and dissolve in the droplet of the liquid phase. The surface of the liquid has a high accommodation coefficient and is therefore preferred for deposition. Upon saturation, the growing particles in the droplet of liquid will diffuse and settle at the boundary between the substrate and the liquid. After precipitation, nucleation takes place and the growth of the crystal subsequently begins. Further deposition and growth will lead to the separation of the substrate and the droplet in such a way that the droplet will be located at the top of the growing crystal, which as a result leads to the growth of NWs.

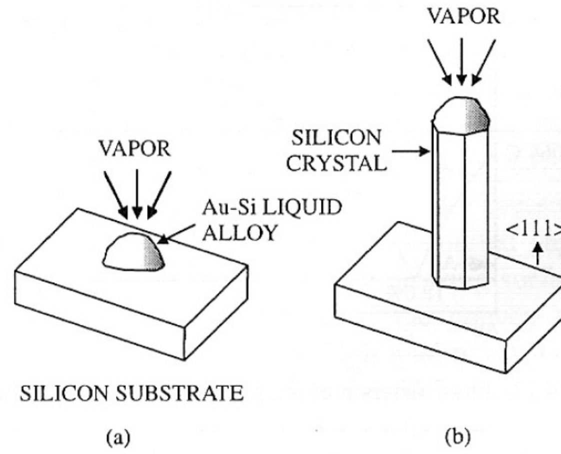

Figure 8. Schematic representation of the main stages of crystal growth using the Vapor-Liquid-Solid Mechanism: (a) initial nucleation and (b) continued growth taken from [36].

Crystalline defects, such as screw dislocations, are not necessary for growth by the mechanism of the VLS. However, defects at the boundary can contribute to growth and reduce the necessary supersaturation. NWs can grow in form of monocrystals, polycrystalline and amorphous materials depending on the substrate and growth conditions.

The equilibrium vapor pressure depends on the energy of the surface and the radius of curvature of the surface, according to the following Kelvin equation [36]:

$$\ln\left(\frac{P}{P_0}\right) = -\frac{2\gamma\Omega}{kTr} \quad \textbf{(3)}$$

In Kelvin equation: P is vapor pressure over a curved surface, P_0 is vapor pressure over an ideally flat surface, γ is surface energy, Ω is atomic volume, r is surface radius, and k is Boltzmann constant.

For the growth of homogeneous high-quality crystalline NWs, the supersaturation of the vapor should be relatively small, thus there will be no growth on the side surfaces. Strong supersaturation will lead to the growth of other faces, as well as with the growth of the crystal from the vapor phase described above. A further increase in supersaturation will lead to secondary nucleation on growth surfaces, as a result of which epitaxial growth will stop.

The diameter of the NWs produced by the VLS method is determined by the size of the catalyst drop. To obtain thinner NWs, it is need to reduce the size of the droplets of the liquid phase. To form small drops of the catalyst, the substrate is usually coated with a thin layer of catalyst material and then annealed at elevated temperatures [41]. During annealing, the catalyst reacts with the substrate to form a eutectic, which leads to a decrease in the total energy of the

surface. A typical example is the use of gold as a catalyst and silicon as a substrate. The size of the catalyst droplets can be controlled by varying the thickness of the catalyst film on the substrate. In general, the thinner the film, the smaller the droplets are formed, which leads to the growth of NWs of smaller diameter [42], as shown in Figure 9.

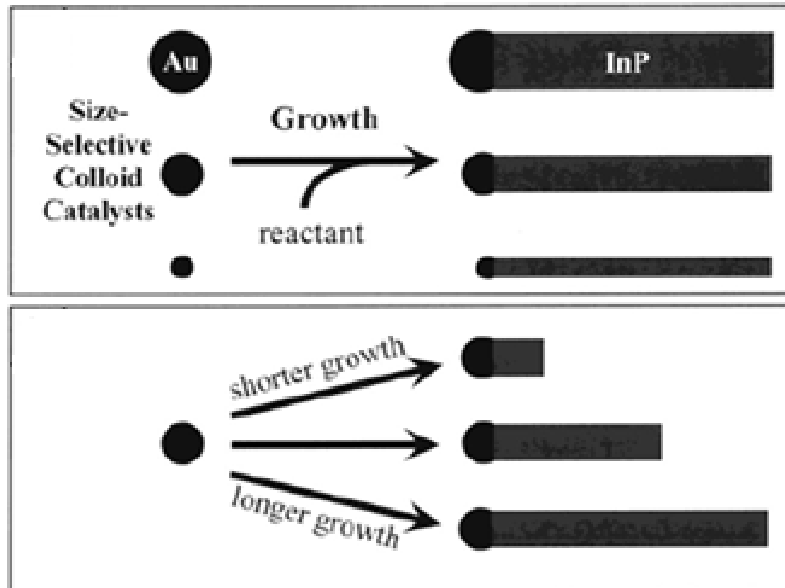

Figure 9. A diagram illustrating a general idea of the diameter and length control of NWs by varying the size of the catalyst droplet and the growth time, respectively [42].

VSL method allows use a large number of materials for growth, such as group III–V (GaAs, GaP, InAs, InP, etc.), II–VI materials (ZnS, ZnSe, CdS, etc.) and nitrides. The flexibility of this method makes it dominant for creating NWs. In the case of compound material NWs, their growth is usually provided by metal–organic chemical vapor deposition (MOCVD) [35].

1.3.3. Template Synthesis

Template synthesis of nanostructured materials is a common method to obtain nanorods and NWs of polymers [43-44], metals [45], semiconductors [46] and oxide materials [47]. For this purpose, various templates with nanochannels are used. The most commonly used and commercially available templates are membranes of anodized aluminum oxide [48] and polymeric membranes [49]. Also as templates nanochannel array glasses [50], mesoporous materials [51], porous silicon obtained by electrochemical etching [52], or carbon nanotubes [53] are used. Figure 10 shows SEM images of NWs, which were obtained by template synthesis method.

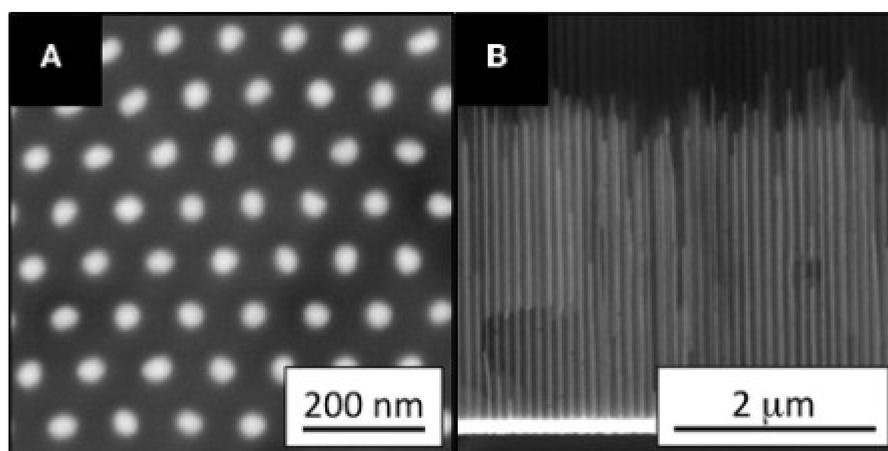

Figure 10. SEM images: a) Template from anodic aluminum oxide filled with cobalt, b) An array of cobalt NWs obtained by the method of template synthesis taken from [54].

In addition to the desired size of pores or channels, morphology, distribution of pore size and density, other requirements are imposed on the template material. First, the template material must be compatible with the processing conditions. For example, in electrochemical deposition, a dielectric must be used as a template material. The template material must be chemically and thermally inert during the synthesis. Secondly, the deposited material or solution should completely wet the pore walls. Thirdly, for the synthesis of NWs, precipitation should begin at the bottom or edge of the template channels and continue from one side to the other.

2. METHODICAL PART

It is obvious that semiconductor NWs built into micro- and nanostructures can experience considerable mechanical stresses. In order to avoid possible destruction of the NWs, there is a need to secure their elastic characteristics. They are not known, so it is needed to examine them, in particular to define Young's modulus.

To study NWs of gallium phosphide, several methods of analysis that allow obtaining data of the geometric characteristics and properties of the material have been chosen. These methods included optical microscopy, SEM, and AFM.

2.1. Scanning Electron Microscopy

In 1935, M. Knoll formulated the idea of constructing an electron microscope [55]. According to this idea, the image of the object is formed sequentially by points and represents the result of the interaction of the electron beam (probe) with the sample surface. Each point of the sample is sequentially irradiated by a focused electron beam, which moves along the surface being studied similarly to the scanning of an electron beam in television systems. During interaction of probe electrons with matter, response signals of different physical nature (reflected and secondary electrons, Auger electrons, X-ray radiation, light, absorbed current, etc.) arise which are used for synchronous imaging on the monitor screen.

Until now, there is no real alternative [56] to this microscopic method to observe the surface from the point of view of high spatial resolution (in modern instruments up to angstroms [57]), and considerable depth of field. Moreover, SEM allows to form images with extremely high speed due to scanning electron beam, and to conduct a local chemical analysis based on recording the characteristic X-ray.

The electron microscope has the following advantages: the first advantage of SEM is that it allows to investigate large surface areas on massive samples in a wide range of magnifications from 10 to 50,000 and higher with high resolution. At the same time, it is not typically required (as for the TEM) to perform complex and lengthy operations to prepare samples before scanning. Secondly, with SEM, one can investigate the entire surface of the object with small magnifications and study in detail any region of interest with large magnifications. The transition from small magnifications to large ones on the SEM is quick and easy. The next advantage is large depth of focus, which makes it possible to observe a three-dimensional image of the structure with the possibility of its quantitative evaluation. Also, SEM is usually equipped with

microanalyzers of chemical composition, which allows to obtain more complete information about the surface of the sample.

The device consists of four main blocks, when working together creating an image of an object: electron gun, lens system forming an electronic probe, sweep generator and secondary radiation detectors. Figure 11 shows schematic construction of SEM.

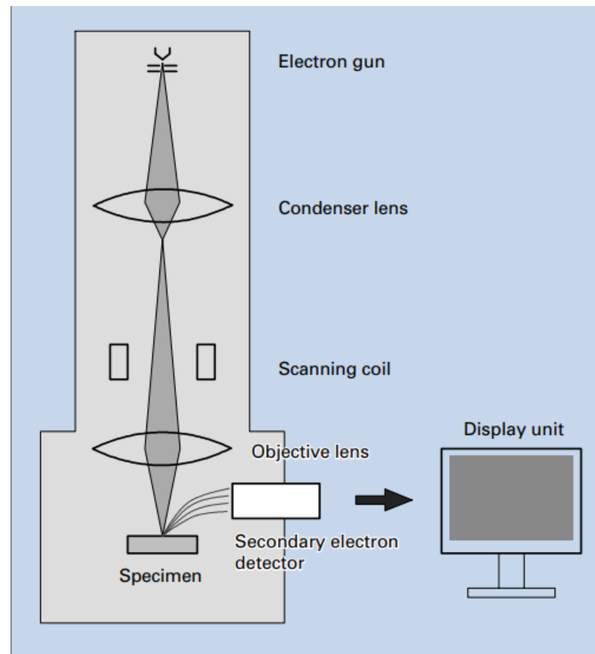

Figure 11. Basic construction of a SEM taken from [58].

The electron beam, emerging from the electron gun, is focused in such a way that its dimensions in the plane of the object under study will be as small as possible. An electron gun containing a thermionic cathode or field emission cathode as an electron source accelerates them to a given energy and converts them into a spot of small diameter, from which the beam diverges at a small angle and passes several electromagnetic lenses. Lenses project a spot with a significant decrease to the surface of the object, forming an acute-focused probe. Electrons, getting on the object, interact with the substance of the near-surface layer and cause various effects, accompanied by the emission of secondary electrons, by X-ray and light (cathodoluminescent) radiation.

As a result of the interaction of primary electrons with the sample (substance), different signals are generated. The main ones are the flow of electrons: reflected, secondary, Auger electrons, absorbed, transmitted through the sample, and also radiation: cathodoluminescent and X-ray (Figure 12).

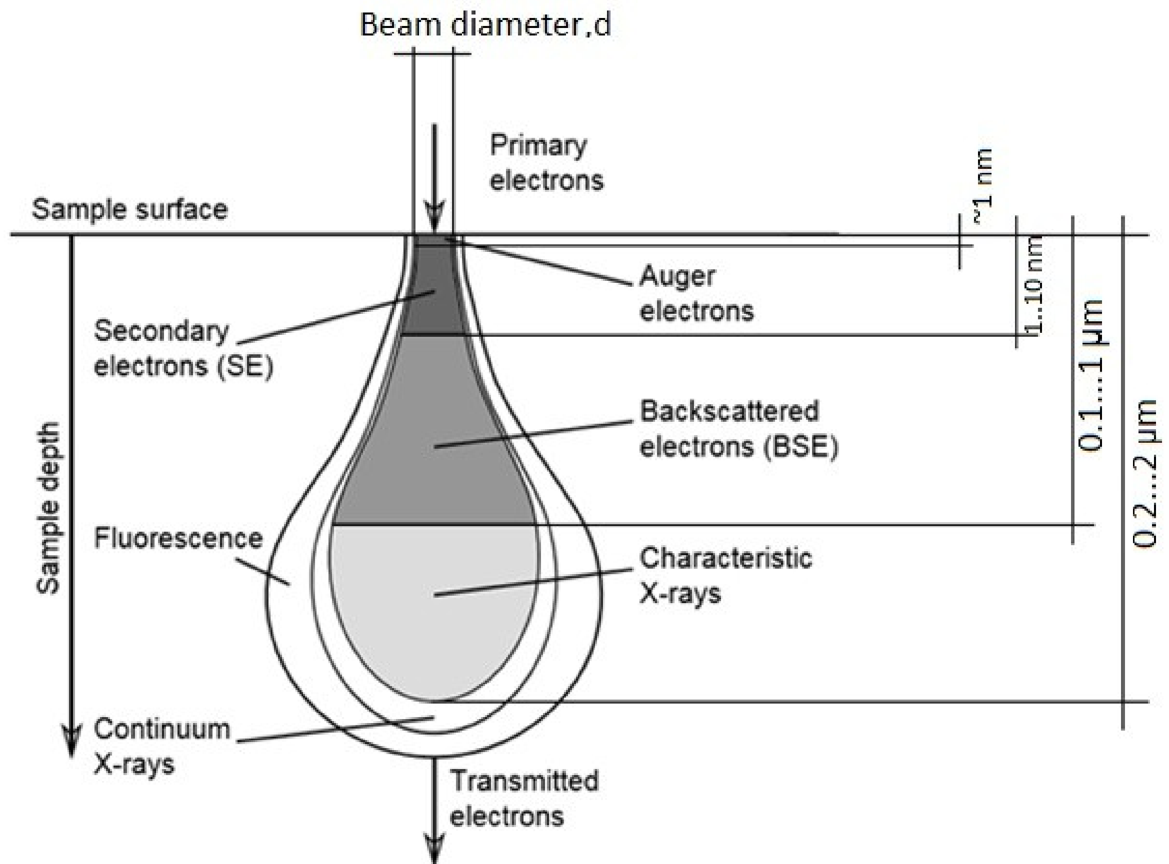

Figure 12. Areas of signals, when the surface of the sample is irradiated with an electron beam.

The main detector detects electrons, converts them into an electrical signal, which after amplification arrives at the monitor, controlling the brightness of the current pixel element. Using the scan generator and deflection system, the electron beam scans the surface of the object, forming a raster. The signal at the output of the detector changes as the probe moves from point to point, displaying structure element by element. This signal, modulating the brightness of the conjugate pixels on the monitor screen, creates an image of the object.

Simultaneously with the motion of the electron beam, the conjugate image element is displayed on the screen. The brightness of the element is determined by the level of the detector signal. The picture on the screen shows the value of the secondary electron emission from the surface of the sample.

To avoid collisions of electrons with gas molecules, their flight from the gun to the object must pass under conditions of high vacuum, which is provided by a two-stage pumping system. In SEM the most common modes of operation are two: the formation of contrast in reflected and secondary electrons.

In the study of NWs, the use of SEM helps to assess degree of coating of the substrate with NWs, their diameter, and the location of single spaced NWs, which is important in case of mechanical characteristics study. This information is later combined with optical microscopy and AFM data to calculate the Young's modulus of NWs using the Euler-Bernoulli beam theory.

2.2. Atomic Force Microscopy (AFM)

Scanning probe microscopes (SPM) are devices designed to study various surface properties by means of solid pointed probes (cantilevers) in the process of scanning sample and a cantilever mutual displacement according to predetermined algorithms. Any SPM consists of a solid probe, a scanner that provides the displacement of a probe and a sample in three coordinates, a probe and sample delivery system, an analytical signal recording system, an electronic data management and reading system, an information recording and processing system, and a vibration protection system. AFM is one type of SPM, which is specified by G. Binnig and G. Rohrer. In 1986, G. Binnig and G. Rohrer were awarded the Nobel Prize for the development of the principles of Scanning Tunneling Microscopy (STM) and AFM.

In the method of AFM, is recorded the force interaction of two bodies. At large distances, the main contribution to the force interaction of two electrically neutral bodies is made by the interaction of fluctuation dipole moments (Van der Waals interaction). At small distances, the exchange repulsion due to the Pauli principle predominates (Figure 13).

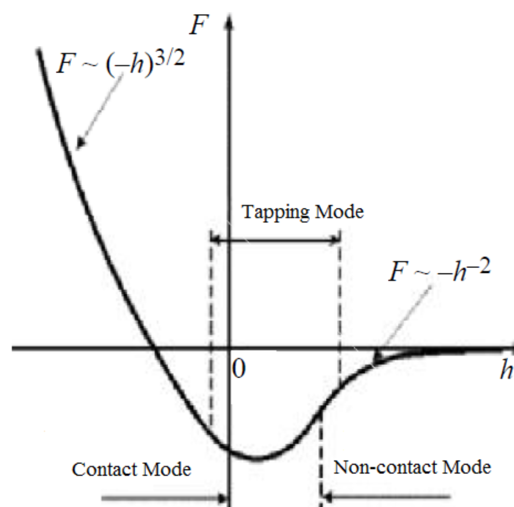

Figure 13. Dependence of the interaction force on the distance between the needle and the surface of the sample. "0" is the boundary of the contact mode in the AFM [59].

By using AFM it is possible to obtain nanometer and atomic resolution [59] images of the surface of both conductive and non-conductive materials. A distinctive feature of AFM, in addition to high resolution, is the possibility to obtain three-dimensional image of the surface, and the possibility of obtaining quantitative information about its electrical, tribological, mechanical and other characteristics.

AFM scans the surface of a sample with a thin probe, the length of which is usually several micrometers, and the diameter is less than 10 nm. The probe is located at the free end of the cantilever with a length of 100 to 200 μm. Figure 14 presents the parts of AFM probe.

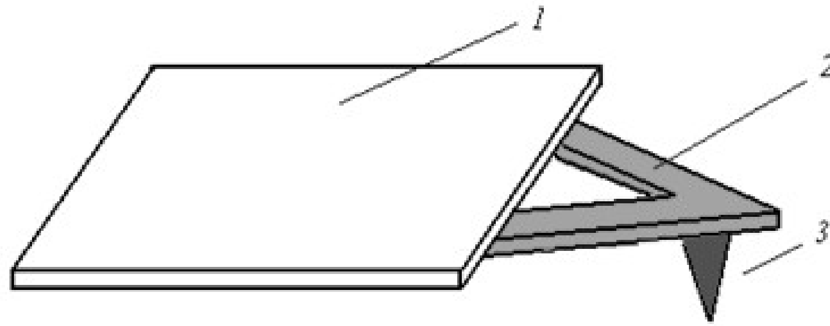

Figure 14. Image of cantilever and tip: 1 is the rectangular base (substrate); 2 is the A-shaped cantilever; 3 is a pyramidal probe (tip).

As the distance between the cantilever and the sample decreases, the repulsive forces sharply increase, which leads to the cantilever bending. For the interaction of two neutral atoms, the total pair potential energy reflecting this effect is described by the Lennard-Jones potential:

$$U_{12}(R) = \mathcal{E}_{12}\left\{\left(\frac{\sigma_{12}}{R}\right)^{12} - \left(\frac{\sigma_{12}}{R}\right)^{6}\right\} \quad \textbf{(4)}$$

σ_{12} is the equilibrium distance (Van der Waals radius) and $\mathcal{E}_{12}$ is the depth of the potential well at the minimum point.

The coefficient at R^{-6} is expressed in terms of the atomic polarizabilities of the first and second atoms.

A special detector registers the deviation of the cantilever as the tip moves along the surface of the sample. A four-section is the most commonly used photodetector as the recording element in AFM. It allows recording both changes in the cantilever's inclination (normal displacement) and its axial bends – lateral forces. The obtained data with the help of a computer make it possible to construct a topographic image of the surface. Figure 15 shows: laser (1), cantilever with a tip (2), sample (3), four-section photodetector (4), piezoelectric tube (5), and

feedback unit (6). At present, almost all AFM piezoelectric tubes are made in the form of piezoceramic tubes with a special configuration of electrodes [60].

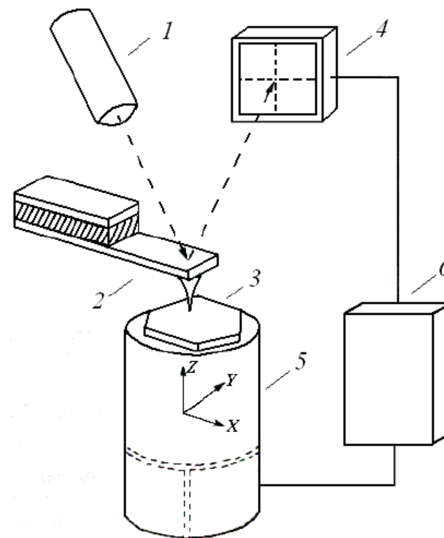

Figure 15. Schematic diagram of the AFM scanning unit with registration of cantilever deflection by reflected laser beam deflection taken from [59].

The optical system of the AFM is aligned in such a way that the radiation from the laser is focused on the console of the probe sensor, and the reflected beam enters the center of the photosensitive region of the photodetector, as shown in Figure 16. The main parameters recorded by the optical system are the bending deformations of the cantilever under the action of the Z-components of the forces of attraction or repulsion (F_Z) and torsion deformation of the cantilever under the action of the lateral forces (F_L) components due to interaction of the probe with the surface.

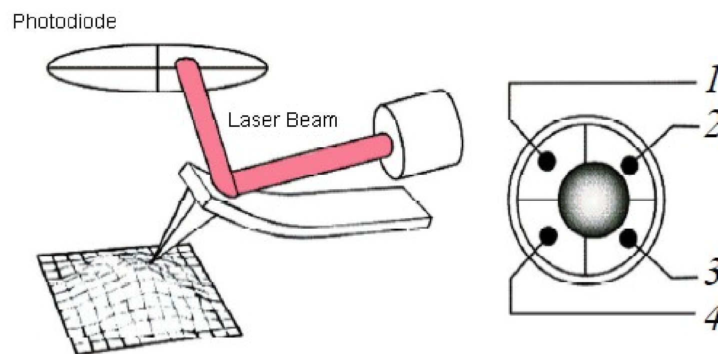

Figure 16. Schematic representation of a sensor and a scheme for optical recording of cantilever bending; 1 ... 4 are photodiode section numbers [59].

If the initial values of the photocurrent in the photodiode sections are denoted by I_{01}, I_{02}, I_{03}, I_{04}, and the currents values after the console position change by I_1, I_2, I_3, I_4, the difference of the currents from different photodiode sections $\Delta I_i = I_i - I_{0i}$ will characterize cantilever's bending value and direction.

The difference of currents, ΔI_Z, is proportional to the bending of the cantilever under the action of a force directed along the normal to the surface of the sample:

$$\Delta I_Z = (\Delta I_1 + \Delta I_2) - (\Delta I_3 + \Delta I_4). \quad \textbf{(5)}$$

The difference of currents, ΔI_L, currents characterizes the bending of the cantilever under the action of lateral forces:

$$\Delta I_L = (\Delta I_1 + \Delta I_4) - (\Delta I_3 + \Delta I_2). \quad \textbf{(6)}$$

Figure 17 presents the Feedback System (FB) of AFM. The value of ΔI_Z is used as an input parameter in the feedback loop of an atomic force microscope. FB provides ΔI_z = const by means of a piezoelectric actuator that supports the bending of the system ΔZ to the value of ΔZ_0 given by the operator.

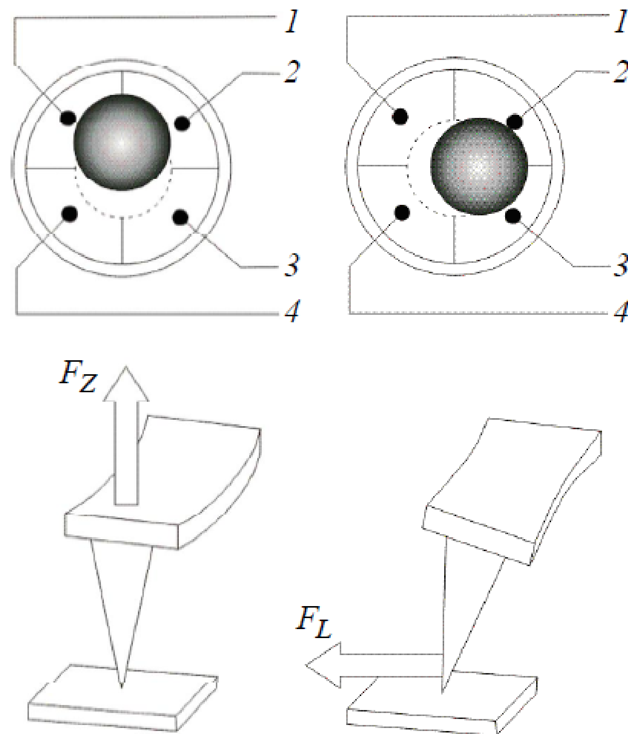

Figure 17. The correspondence between the type of flexural deformations of the cantilever and the change in the position of the spot on the photodiode [59].

When scanning the sample in the ΔZ = const mode, the probe moves along the surface, and the voltage at the Z-electrode of the scanner is recorded in the computer's memory as a surface relief $Z = f(x, y)$.

The probe moves along the line firstly in the forward direction, and then in the opposite direction, then goes to the next line. The obtained data with the help of a computer make it possible to construct a topographic image of the surface.

2.2.1. AFM cantilevers

One of the most significant things when working with an atomic force microscope is a probe, a detail that does not even refer to the measuring instrument itself. During operation, the probes have to be changed frequently enough as they become dull or dirty. In AFM microscopy, much is determined not only by the tip of the probe itself, but also by the cantilever. Therefore, the probe needs to be selected in a proper way, since the right choice determines the quality of the result.

Producers of AFM probes usually produce three versions of geometry: pyramidal, tetrahedral and cone-shaped. Cone shaped probes can be made sharp with a high aspect ratio (length to average diameter ratio). Pyramidal probes have a lower aspect ratio and a curvature nominal radius of several hundred angstroms, but they are more durable. Figure 18 demonstrates different types of AFM probes.

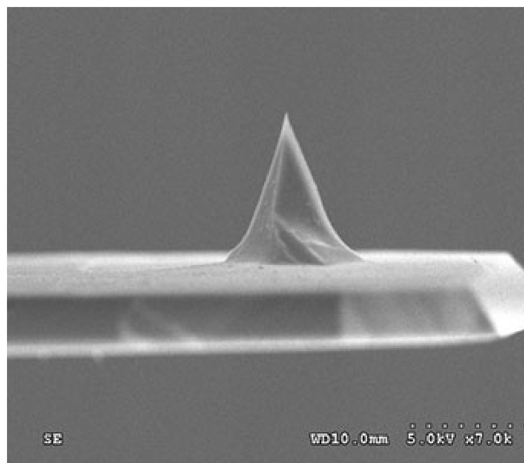

a)

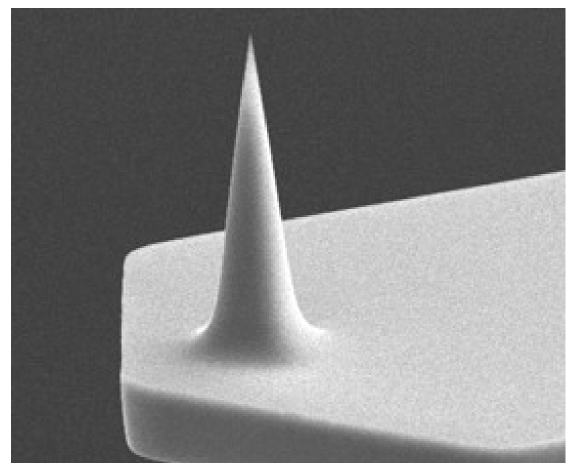

b)

Figure 18. Different types of AFM probes: a) pyramidal, b) cone-shaped [59].

Probes for AFM are made of silicon or silicon nitride. The parameters of the probes depend on the technology of the production, as well as on the properties of the materials

themselves. Cone-shaped silicon probes are made by etching silicon around a mask of silicon dioxide. Silicon can also be doped, which allows to make conductive probes without applying a conductive coating, which would increases tip radius [61].

Probes made of silicon nitride are made by depositing a layer of silicon nitride in an etched groove on the surface of a silicon crystal. Using this method, probes with a pyramidal and tetrahedral geometry are made. The aspect ratio of such probes is limited to the crystallographic structure of silicon. These probes are wider than conical silicon probes. Silicon nitride is a harder material than silicon, which also provides greater durability of silicon nitride probes compared to silicon ones.

Due to a wide variety of the probe types on the market, it is important to correctly select the probe not only for its shape, but also for tip curvature and image step. Consider an image of 512 by 512 points of size 1 by 1 micron. The digit size is then 2 nm. Since the interaction zone between the tip and the sample is part of the radius of the tip curvature, such tips usually provide a horizontal resolution of less than 1 nm. Thus, the resolution of images obtained on AFM more than 1 to 1 micron, depends not on the tip radius, but on the size of the image step. To obtain scans, the size of one point which exceeds the radius of curvature of the tip, it is not appropriate to use sharp or expensive probes [62].

Resolution in SPM and AFM is often determined according to the Rayleigh criterion [63]: two peaks are considered distinguishable in the image if the measured depth of the depression between these peaks is at least 19% of the total height of the peaks.

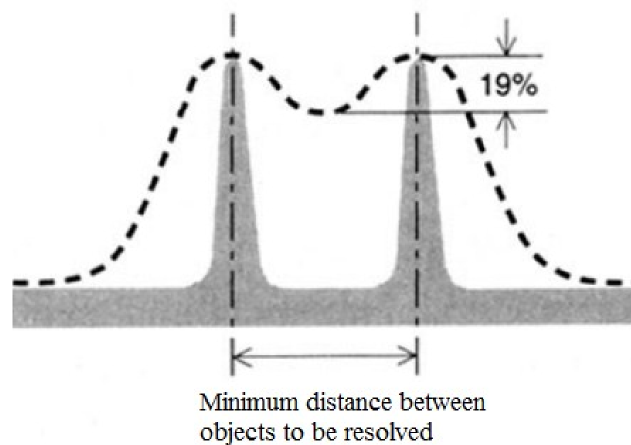

Figure 19. The definition of lateral resolution by the Rayleigh criterion [63].

The minimum distance between different sample's heights determines the maximum lateral resolution of the system. Given this definition, the resolution of AFM, equipped with the sharpest cantilevers available on the market, reaches ~1 nm [63].

The sharpness of the probe plays an important role in the formation of the image. If the tip of the probe is greater than the surface elements, distortion occurs, so-called tip imaging. The tip imaging is contrasted with the true imaging. Each data point in the image represents a spatial convolution of the shape of the tip and the shape of the object to be taken. If the object is larger than the tip, then the image of the edge of the object is displayed on the image. However, if the object is smaller than the tip, the shape of the tip will be dominated in the image. Figure 20 shows the origin of the effect.

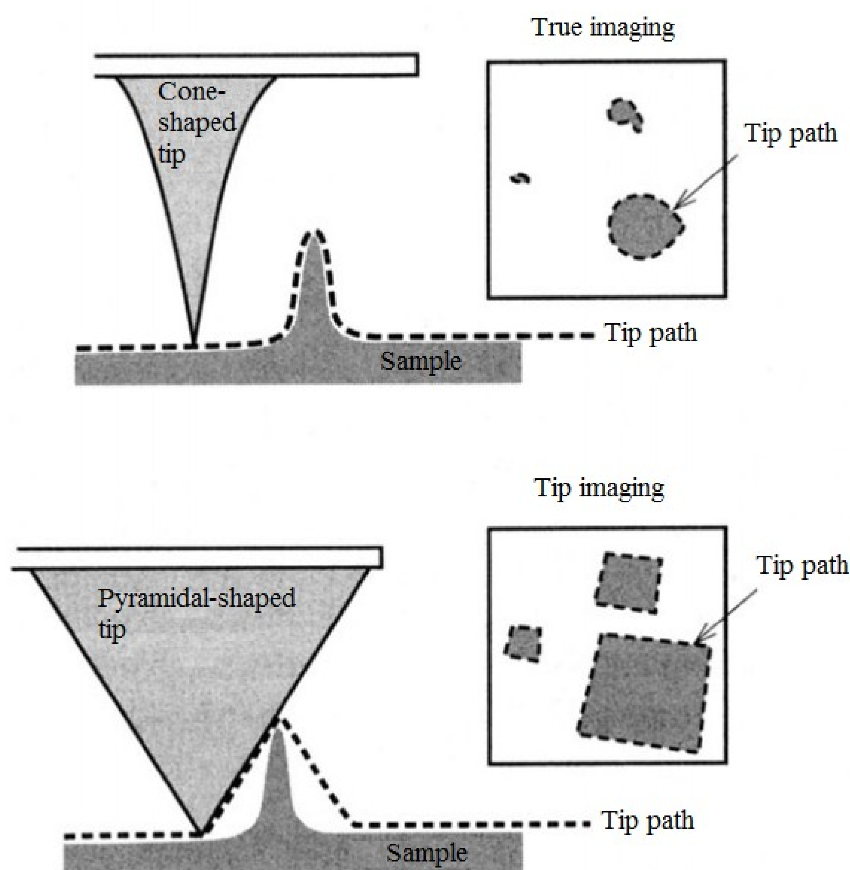

Figure 20. Comparison of the real image with the image in the presence of tip convolution [63].

To determine the presence of a tip convolution, one should search for a characteristic contour that is repeated throughout the image. It can be of different sizes, but will always have the same orientation. More detailed information about this can be found in the following sources [63-64].

2.2.2. PeakForce QNM mode

PeakForce™ QNM (Quantitative Nanomechanical Property Mapping) is a mode that allows AFM users to quantitatively characterize nanoscale materials. It displays and distinguishes nanomechanical properties, including modulus and adhesion, while simultaneously visualizing the topography of a high-resolution sample. PeakForce QNM operates over an extremely wide range, approximately 1 MPa to 50 GPa for modulus and 10 pN to 10 µN for adhesion, enabling characterization of a large variety of sample types.

AVAILABILITY	
Optional Feature	PeakForce QNM is an optional feature on all new Dimension® Icon®, MultiMode®8, and BioScope™ Catalyst™ SPM systems
PROBE RECOMMENDATIONS	
Modulus Range:	
<20 MPa	ScanAsyst-Air (k~ 0.4 N/m nominal, tip radius <10 nm typical)
5 – 500 MPa	Tap150A (k~ 5 N/m nominal, tip radius <10 nm typical)
200 MPa – 2 GPa	RTESPA (k~ 40 N/m nominal, tip radius <10 nm typical)
1 – 20 GPa	Tap525 (k~ 200 N/m nominal, tip radius <10 nm typical)
>10 GPa	DNISP-HS (k~ 350 N/m nominal, tip radius <40 nm typical, diamond tip)
	(A selection of these probes is included with the PeakForce QNM package)
STANDARD SAMPLES	
Modulus: 1 MPa – 100 GPa	Several standard samples are included with the PeakForce QNM package, each covering approximately one order of magnitude of the specified range. These may be used for calibration and as training samples. Note that samples are not certified by any standards agency and may vary with aging.
TYPICAL PERFORMANCE	
General	Absolute accuracy, reproducibility, and resolution vary with the calibration method and measurement procedure. Absolute accuracy is also difficult to specify because of a lack of certified standards. Therefore, guaranteed performance specifications cannot be given at this time. Please refer to the data shown as a guide to typical performance.

Figure 21. Peak Force QNM Specification given by Bruker Company [65].

In order to understand how the QNM works it is necessary to consider Force-versus-time and force-versus-distance curves. Figure 22 shows these curves.

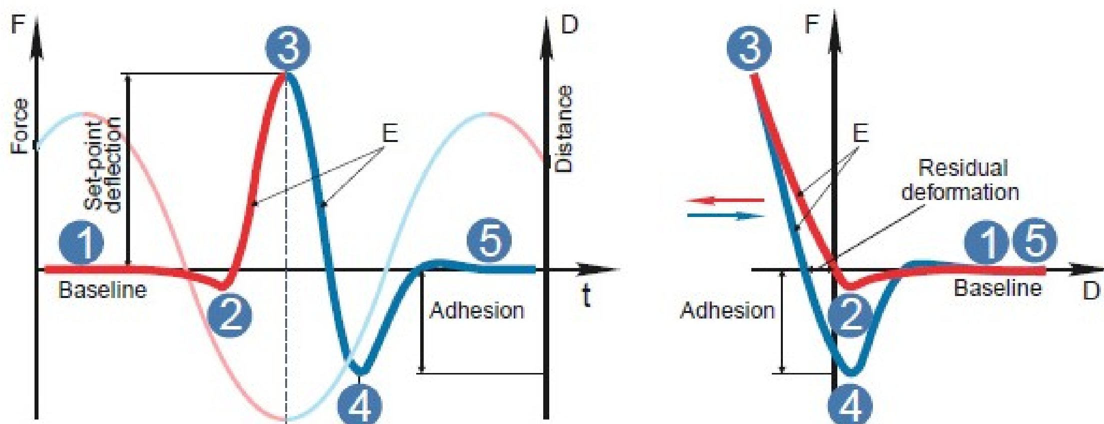

Figure 22. Force-versus-time, Fvt (left), and force-versus-distance, FvZ (right), curves in an oscillatory cycle of the QNM [65].

Figure 22 on the left shows a sine wave that shows a vertical motion of the scanner. This movement begins with the deflection of the probe from the baseline (1), then goes into a slightly attractive (2) and goes until the tip-force reaches a predefined set-point (3). This section is marked in red. hen (marked in blue), a departure from the sample occurs. The probe bending returns to the baseline level (5) passing the adhesive well (4) [46].

2.3. Euler-Bernoulli beam theory

In order to analyze the data obtained by AFM and SEM, it is necessary to use a theoretical model, which will describe the processes of mechanical deformation occurring in NWs. The process of measuring mechanical deflections in a NW with the help of AFM bending will be described in Chapter 3.2. in detail, while this chapter will describe the equations that will be used to process the experimental data. In this work, NW will be considered as a single-clamped beam, on which forces of different values are alternately applied.

Figure 23 shows the various ways of fixing the NW or experiment geometries:

a) NW freely grows on the substrate, it can be considered as a single-clamped beam [66];

b) NW is preliminarily separated from the substrate (broken by the AFM probe or cut off by Focused Ion Beam (FIB)) and lies on substrate surface. With the help of the AFM cantilever, a sample is pushed into the surface. This method is also called Nanoindentation [67];

c) NW can be installed over a small groove and fixed with Cu or Pt, which will also help to measure its bending. Such structure can be regarded as a double clamped beam [68];

d) The structure is similar to c), however, the fixation can be absent. For such structure it is rather difficult to determine the boundary conditions [69];

e) The structure is also similar to c), but it is fixed from one end. In the case of tappered NWs, it is possible to fasten the NW at both the wide end and the narrow one;

f) NW can be mounted above the groove, be fixed from one end, and the other one freely hang over the groove. This geometry returns to a) and can be regarded as a kind of single clamped beam.

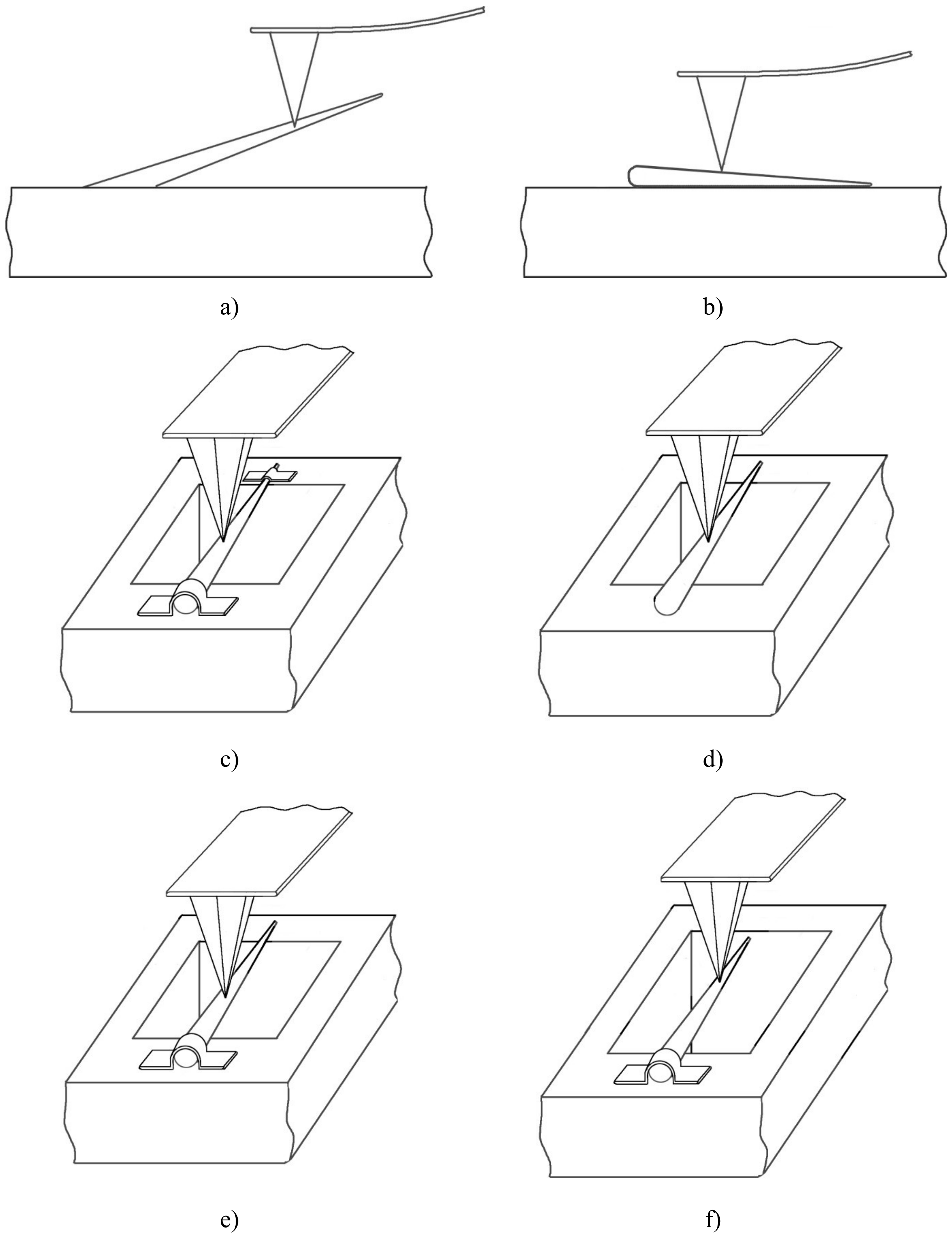

Figure 23. Different experiment geometries.

The measurement of single clamped NWs (Figure 23, a) is, in our opinion, the best, since no modifications are made for the measurement of the NW. As such geometry, the NWs growing freely on the surface of the substrate are considered without further processing and transportation of NWs that can affect the shape of NWs and/or alter their properties.

To describe the behavior of beams, the most popular are the two mathematic models: Euler–Bernoulli beam theory and the Timoshenko beam theory. In the classical Euler–Bernoulli theory it is assumed that:

1) The cross sections of the beam are flat and perpendicular to the axis of the beam before deformation. They remain flat and perpendicular to the deformed axis of the beam during bending.

2) The normal stresses on areas parallel to the axis are negligible. The longitudinal sections resist bending independently, without influencing to each other.

3) The inertia of rotation of the rod element during bending is neglected.

In the Timoshenko beam theory, the inertia of the rotation is taken into account, which leads to a change in the expression for the kinetic energy of the beam. It is also assumed that the cross sections remain flat, but not perpendicular to the deformed axis of the beam [70].

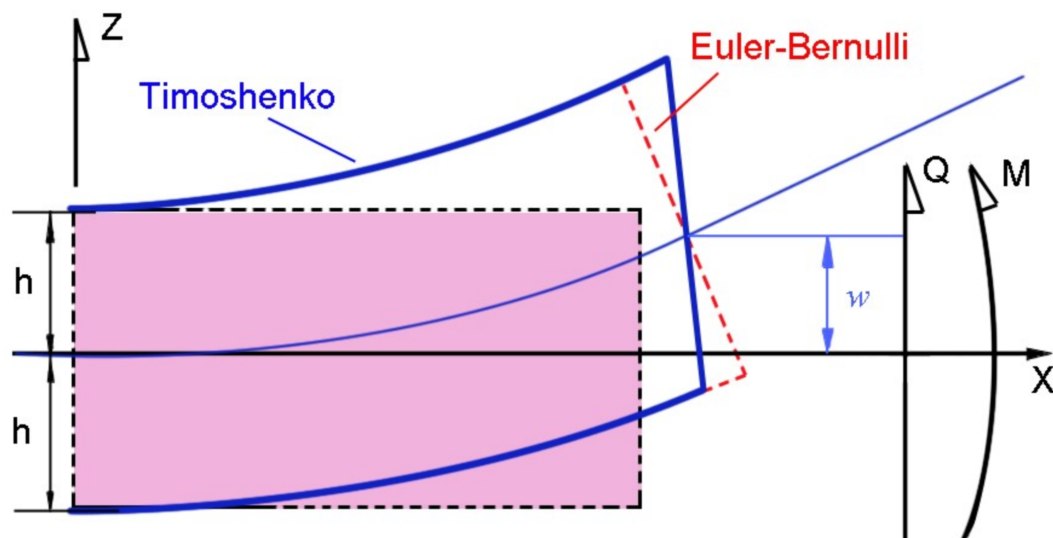

Figure 24. Deformation of a Timoshenko beam (blue) compared with that of an Euler-Bernoulli beam (red).

Figure 24 clearly demonstrates differences in the approaches of Euler-Bernoulli and Timoshenko. In the Euler-Bernoulli beam theory, the cross sections remain perpendicular to the axis of the rod after deformation.

For this work, the Euler-Bernoulli model was chosen, since it is the most simple to consider. However, the classical Euler-Bernoulli theory assumes that a bend will be made over a cylindrical beam. In this work, tapered nanorods were measured. In order to apply the Euler-Bernoulli model to tapered nanostructures, it is necessary to introduce additional parameters that

will take into account the shape of the beam, i.e. the shape of the tapered NW. Dunaevskiy with co-authors [66, 71] derived equations for working with tapered NWs. Let us consider in detail the sequence of derivation of the equation.

To calculate the Young's modulus for conical NWs, Hooke's law and the Euler-Bernoulli theory for a single-fastened beam with a free end are used.

Euler-Bernoulli equation:

$$\frac{d^2}{dx^2}(EI(x)\frac{d^2w(x)}{dx^2}) = 0 \tag{7}$$

Boundary conditions:

$$w\big|_{x=0} = 0 \tag{8}$$

$$\frac{dw}{dx}\bigg|_{x=0} = 0 \tag{9}$$

$$\frac{d^2w}{dx^2}\bigg|_{x=L} = 0 \tag{10}$$

$$\frac{d^3w}{dx^3}\bigg|_{x=L} = \frac{-F}{EI(L)} \tag{11}$$

Where x=0 is for fixed base of NW, x=L is for free end, E is the Young’s modulus of NW, *I(x)* is the second area moment of inertia of the conical NW, L is the length of NW, and *w(x)* is deflection. Using boundary conditions it is possible to obtain the following second order differential equation:

$$EI(x)\frac{d^2w(x)}{dx^2} = -F(x-L)\,. \tag{12}$$

The radius of the NW varies along the length in accordance with the equation:

$$R(x) = R_{mid} + a(x-\frac{L}{2}) = R_{mid}(1+a(x-\frac{L}{2}))\,. \tag{13}$$

Here $a = \frac{\alpha}{R_{mid}}$ is auxiliary coefficient, where α is taper angle. Thus, the second area moment of inertia is given by the following relation:

$$I(x) = \iint_S z^2 dxdy = \int_0^{2\pi} d\varphi \int_0^{R(x)} \rho d\rho \cdot \rho^2 \cos^2 \varphi = \pi \frac{R(x)^4}{4} \quad \textbf{(14)}$$

$$I(x) = \frac{\pi R_{mid}^4}{4}(1 + a(x - \frac{L}{2}))^4 \quad \textbf{(15)}$$

Thus, for the bending of the cone beam:

$$\frac{d^2 w(x)}{dx^2} = \frac{F}{E}\frac{4}{\pi}\frac{1}{R_{mid}^4}\frac{(x-L)}{(1+a(x-\frac{L}{2}))^2}. \quad \textbf{(16)}$$

Using boundary conditions **(8)** and **(9)** for $x = 0$ one obtains the deflection profile as follows:

$$w(x) = \frac{4}{\pi}\frac{F}{E}\frac{1}{R_{mid}^4}\frac{8x^2(-3aL^2 - 2x + L(6+5ax))}{3(-2+aL)^3(-2+a(L-2x))^2}. \quad \textbf{(17)}$$

Despite the fact that all equations are derived in accordance with [72], they must be carefully checked, especially **(17)** and **(18)**. The bend at the end of the NW is given by the formula:

$$\frac{w(L)}{F} = \frac{4}{3\pi}\frac{1}{E}\frac{L^3}{R_{mid}^4}\frac{1}{(1+\frac{aL}{2})(1-\frac{aL}{2})^3} \quad \textbf{(18)}$$

At the same time, Hooke's law states:

$$F = k\delta \quad \textbf{(19)}$$

Where: k is linear stiffness coefficient (spring constant), δ is deformation, and F is force acting on the same axis with deformation.

For the NWs which are bended down by specific setpoint force:

$$F = k_{NW}(x) \cdot w_{NW,F(x)} \quad \textbf{(20)}$$

Spring constant is inversely proportional to flexibility coefficient f:

$$k = \frac{1}{f} = \frac{F}{w_{NW,F(x)}} \quad \textbf{(21)}$$

Thus, from **(18)** and **(21)**:

$$f(x) = \frac{1}{k(x)} = \frac{4}{3\pi}\frac{1}{E}\frac{1}{R_{mid}^4}\frac{x^3}{(1+a(x-\frac{L}{2}))(1-a(x-\frac{L}{2}))^3} \quad \textbf{(22)}$$

At the same time, if we use the coefficient $a_1 = \frac{\alpha}{2R_{mid}} = \frac{\alpha}{D_{mid}}$, we get:

$$f(x) = \frac{1}{k(x)} = \frac{64}{3\pi}\frac{1}{E}\frac{1}{D_{mid}^4}\frac{x^3}{(1+a_1(2x-L))(1-a_1L)^3} \qquad \textbf{(23)}$$

And, eventually thus:

$$\mathrm{E} = \frac{64}{3\pi}\frac{1}{f(x)}\frac{1}{D_{mid}^4}\frac{x^3}{(1+a_1(2x-L))(1-a_1L)^3} \qquad \textbf{(24)}$$

Using experimental data on the deflections of NWs and equation **(24)**, it is possible to calculate the Young's modulus of the GaP NWs.

3. EXPERIMENTAL PART

AFM PeakForce QNM is a unique tool that allows to obtain not only information about the topography of nano-objects, but also to monitor the dynamics of changes in their elastic properties (that is, the Young's modulus) due to the possibility of precise control of the force acting between the sample and the probe. The essence of the PeakForce QNM is that at each measurement point the probe presses the sample with a given force, and then withdraws to a safe distance, then moves to the next point and the cycle repeats again. As a result of this approach, AFM scanning can be performed without damaging the sample. This chapter describes a technique for measuring the elastic properties of nanostructures of GaP using the AFM PeakForce QNM.

3.1. Technological parameters for GaP NWs

Samples were grown in Aalto University by Ms.Sc. Vladislav Khayrudinov. All samples were synthesized on p-Si (111) substrates using MOVPE. Samples differed in shape, diameter, length, and density of coating on the substrate. Information on the samples is summarized and given in Table 1.

Table 1. Description of the samples.

Sample #	Substrate	Material	Length, µm	Shape	Diameter, nm
254	p-Si (111)	GaP	5	Tapered	40...70
261			3-4	Cylindrical	40
262			1-1.5	Tapered	50…140

For these samples, photoluminescence spectra were measured in the range from 1.4 to 2.6 eV. The obtained spectra are shown in Figure 25. According to Figure 25, all samples contain both wurtzite and zincblende phase. From the photoluminescence intensity, it can be seen that in sample 254 the wurtzite phase is greatest, and in sample 261, the smallest. The photoluminescence intensity of sample 262 is slightly less than at 254, but still is at a rather high level, which indicates a large content of the wurtzite phase.

Since in this work we were interested in obtaining data about NWs with a high content of the wurtzite phase, it was necessary to choose between samples 254 and 262.

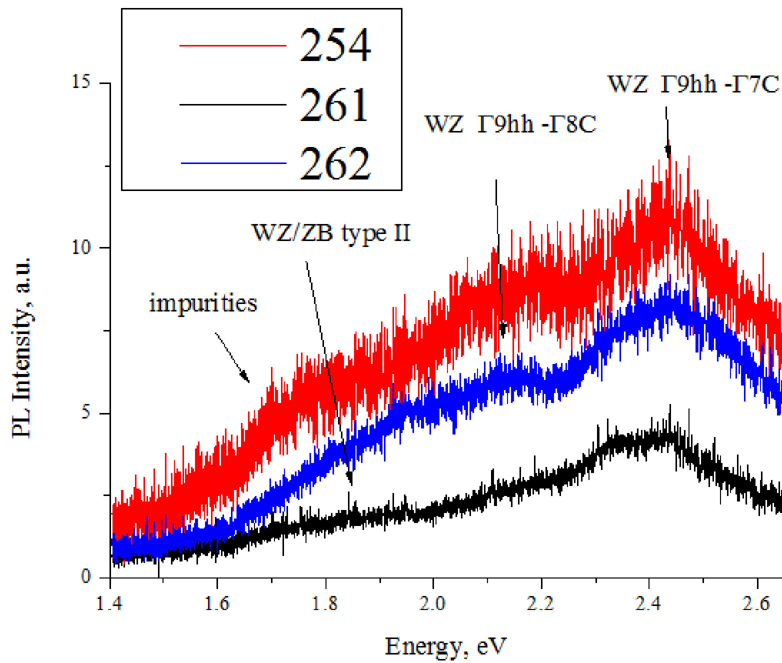

Figure 25. Photoluminescence spectra of GaP NWs obtained with different technological conditions.

Figure 26 shows the SEM images of the surface of samples 254 and 262. According to SEM images, sample 254 is more densely coated with NWs. At the same time, on the sample 254 the NWs are longer and thinner than at 262.

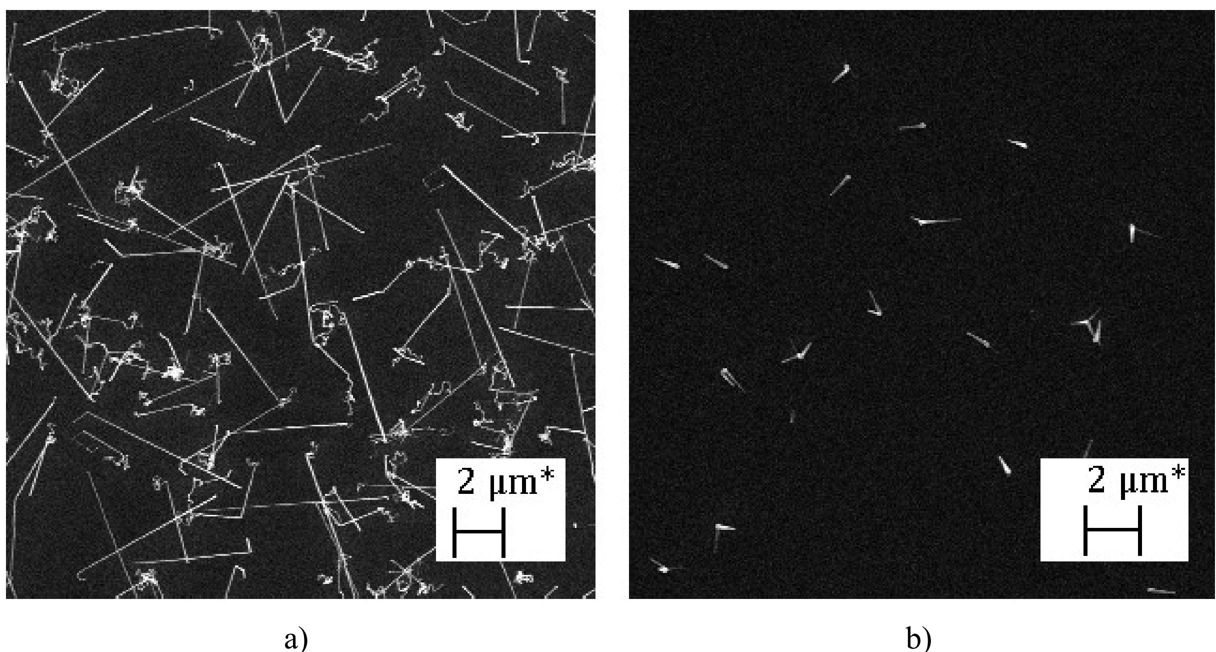

a) b)

Figure 26. SEM images of GaP NWs: a) sample 254, b) sample 262.

Since the sample 262 has a lower degree of coating of the substrate by NWs and the NWs thereon are located at a considerable distance from each other, this sample will be easier to examine on the AFM. For AFM probe it will be easier to bend individually standing NWs, since the nearby objects will not interfere with the measurement. Based on a comparison of the

photoluminescence spectra for several samples and SEM data, sample 262 was selected for further work.

Sample 262 GaP NWs were synthesized on p-Si (111) substrates using MOVPE, as was mentioned before. The sample was first cleaned inside an ultrasonic bath by soaking in acetone and in isopropanol for 2 min, followed by a 2 min rinse in deionized water. 40 nm diameter gold nanoparticles (NPs) from a colloidal solution (BBI International, UK) were used as catalysts for the VLS growth. Poly-L-Lysine solution was applied to the substrate for 10 s for better NPs adhesion followed by 10 s deposition of gold NPs. Prior to the growth, the substrate was annealed in situ at 650°C for 10 min under hydrogen flow to desorb surface contaminants. Growth step was started by switching on the trimethylgallium (TMGa) and tertialybuthylphosphine (TBP) sources simultaneously for 30 s at a fixed growth temperature of 550°C. The nominal V/III ratio during the growth was ~100, and the TMGa and TBP flows were 5.36 and 550 μmol/min, respectively. After the growth only the TBP flow was kept on during the reactor cooling down to 250°C. SEM images of the obtained NWs are shown in Figure 27. More details about the growth process can be found in [73-74].

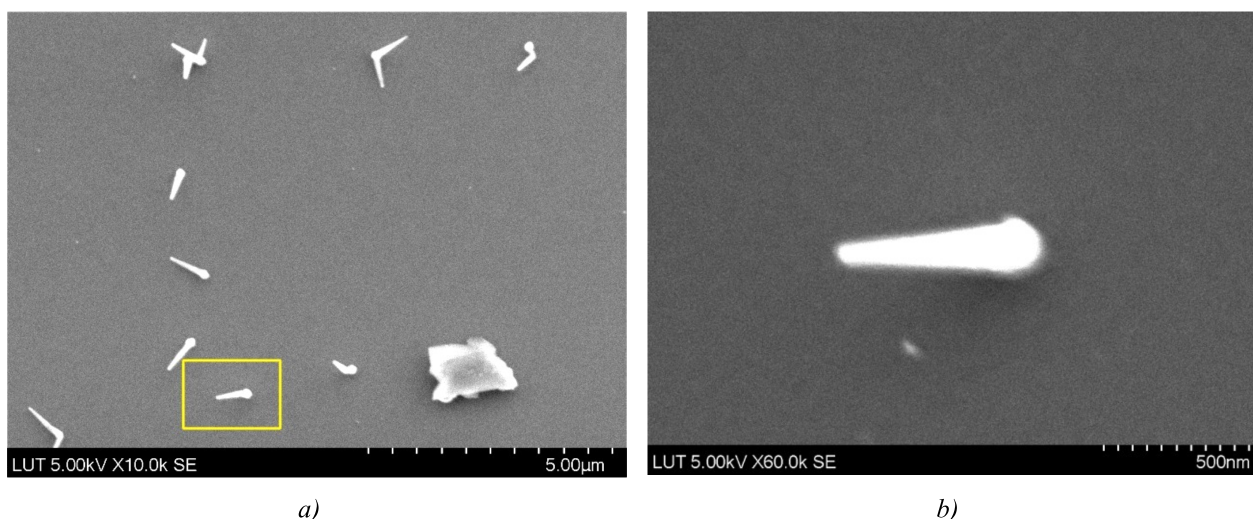

a) *b)*

Figure 27. SEM images of GaP NWs: a) location on the substrate, b) individually standing NW, conical shape is visualized.

It is noticeable, that the NWs have conical shape with an average diameter ranging from 50 to 140 nm, and length of 1-1.5 μm. The NWs have a taper angle of ~3 degrees.

3.2. Measurement Procedure

This chapter describes step-by-step actions for measuring the mechanical properties of NWs using AFM Bruker MM8 in the PeakForce QNM.

Step 1 about 10 – 15 min. When starting measurements it is needed to **calibrate** a new probe. When the probe has been already calibrated, move to step 2. Despite the fact that probes for AFM from one kit have close parameters for operation, a calibration procedure must be carried out for each new probe.

1. Install the probe into the probe holder. Installation of the probe into the probe holder is performed by the operator with his own hands using tweezers. It is recommended that each probe is placed in the same position, guided along the probe holder edges.

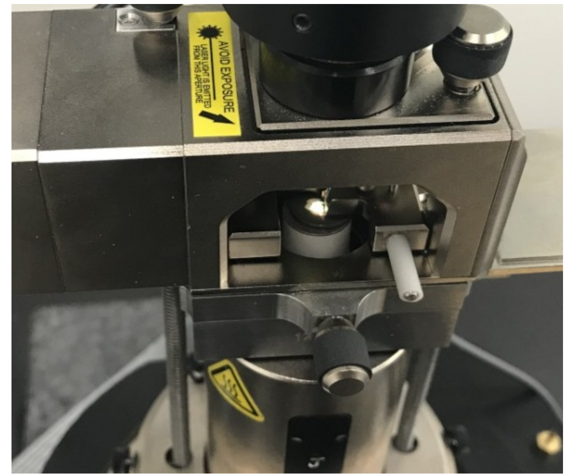

a) b)

Figure 28. a) AFM probe holder with installed probe; b) In progress.

2. Install reference sample in accordance with probe (Figure 29). The placement of any sample in the AFM should be done with great care, in order to avoid damage to the piezoelectric tube, above which the sample is placed.

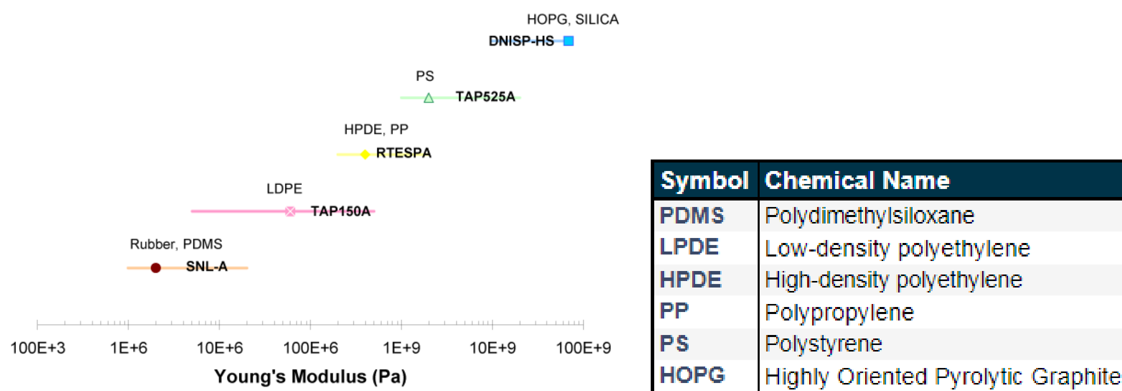

Symbol	Chemical Name
PDMS	Polydimethylsiloxane
LPDE	Low-density polyethylene
HPDE	High-density polyethylene
PP	Polypropylene
PS	Polystyrene
HOPG	Highly Oriented Pyrolytic Graphite

Figure 29. Modulus ranges covered by various probes. The modulus of the reference sample for each range is indicated as well.

3. After installation, the probe locates at a considerable distance from the sample. In order to start calibration, it is necessary to bring the probe closer to the sample surface. To do this, first one need to focus on the surface of the sample using an optical microscope built into the system. Then, to focus on the probe. After that, go back to focusing on the sample's surface and move slowly the AFM's head down until the outline of the probe will be visible as shown at Figure 30.

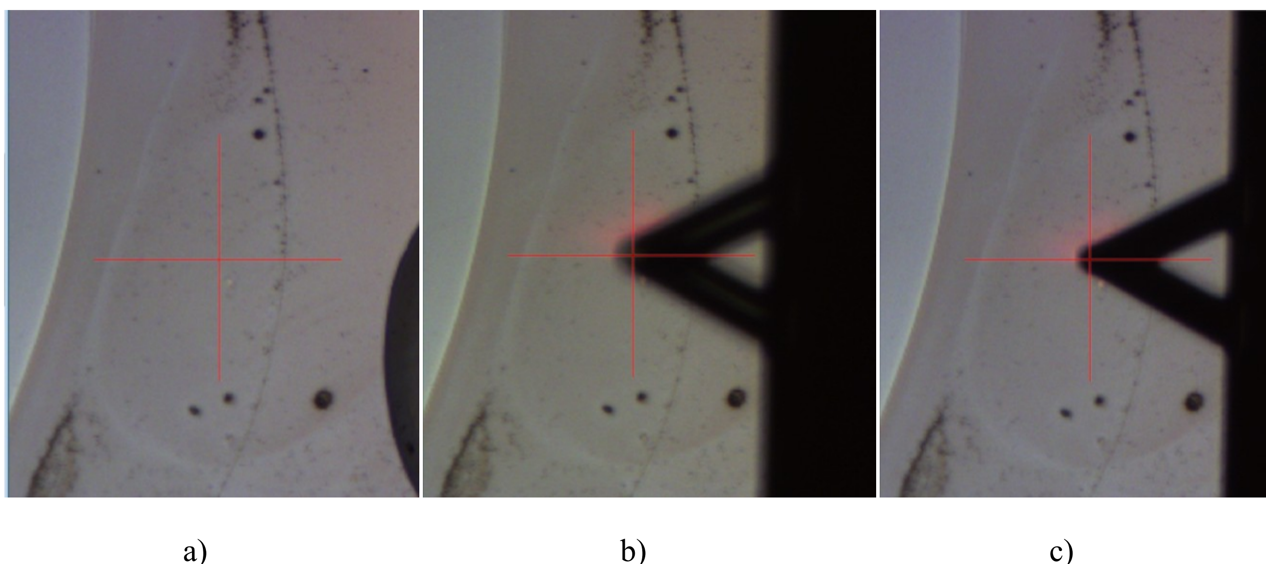

a) b) c)

Figure 30. Optical microscopy window: a) no probe installed, b) the probe is out of focus, the probe on a considerable distance from the sample's surface, c) the probe is almost in focus, the probe is at a small distance from the sample surface.

Make the calibration of SUM (~5-7), VERTICAL (~0) and HORIZONTAL (~0) placement of the laser beam and position of the photodetector at the four-section photodetector by scrolling the knobs. All needed knobs are presented at Figure 31. The calibration starts with the value of the SUM, the value of the SUM should be maximum.

Scrolling the knobs 1 and 2 to its limits, the operator fined this value. That is, the SUM values on the display will be displayed from zero, grow, pass through a maximum, then fall back and go to zero. It is necessary to set knob 1 and 2 to the position at which the sum reaches the maximum. By adjusting knobs 1 and 2 one calibrates the position of the laser. Then it is necessary to proceed to the calibration of the photodetector position by adjusting knobs 3 and 4. Knob 3 adjusts the position vertically, and knob 4 horizontally. The values of both on the display should be approximately equal to zero.

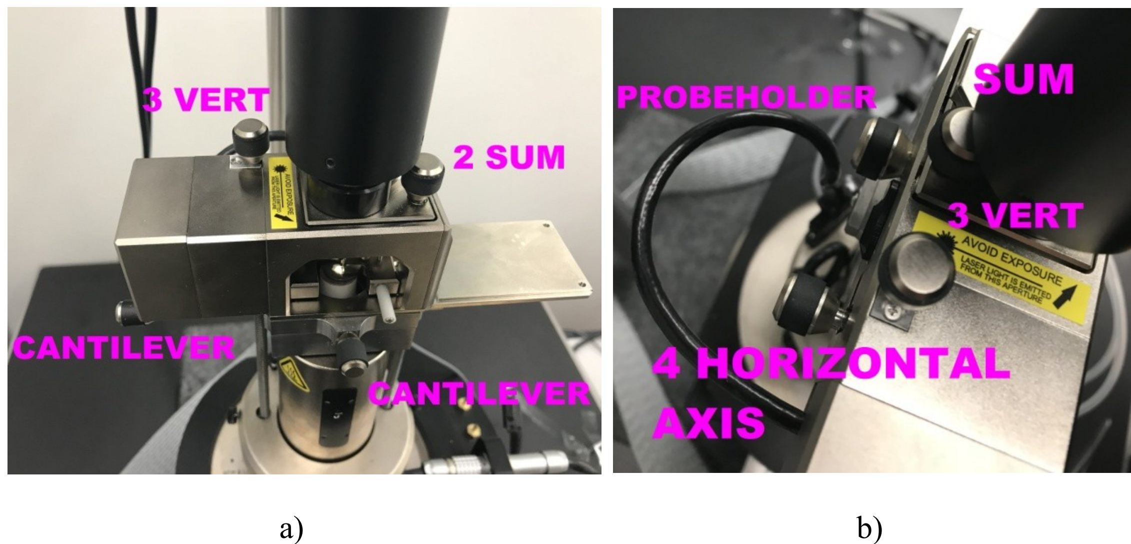

a) b)

Figure 31. Placement of AFM knobs.

For more detailed settings, the operator can use the help of the software and maximize the amplitude of the probe swinging using laser position adjusters.

Now one can move to calibration of **Deflection Sensitivity**.

4. Click the **Select Experiment icon.** This opens the Select Experiment window;
5. Click the **Mechanical Properties** in the **Experiment Category** panel;
6. Select **Nanomechanical Mapping** in the **Select Experiment Group** panel;
7. Select **PeakForce QNM in Air** in the **Select Experiment** panel and click **Load Experiment;**
8. Change **Scan Size** to 0 nm. **Engage** the probe onto a reference sample. Click **Ramp;**
9. Enter the following parameters in panels **Ramp** and **Trigger**;

Parameter	Setting
Ramp output	Z
Ramp size	100 nm–1.00 µm
Scan Rate	1.00 Hz
Number of samples	512

Parameter	Setting
Trigger mode	Relative
Trig threshold	0.2 V

Parameter	Setting
Data Type	Deflection Error
X Data Type	Z
Display Mode	Deflection Error vs. Z

a)

Ramp	
Ramp Output	Z
Ramp Size	100.0 nm
Ramp Rate	1.00 Hz
Forward Velocity	201 nm/s
Reverse Velocity	201 nm/s
Speed Increment Max	3.00 µm/s
Samples/Ramp	512
Retracted Delay	0.00 s
X Rotate	0.00 °
Trigger	
Trigger Mode	Relative
Data Type	Deflection Error
Trig Threshold	5.190 nm
Threshold Safety	7.785 nm
Baseline Fit	30.0 %
Baseline Extrapolation	30.0 %

b)

Figure 32. a) The parameters given in the user's manual, b) the real window in the working software.

10. In the same window to the right of the settings is a Deflection vs. Z plot. The plot shows the dependence of the interaction force between the probe and the sample surface on the distance between them. In the software one need to arrange the cursors so that they surround the contact (steepest) portion of the graph as shown at Figure 33.

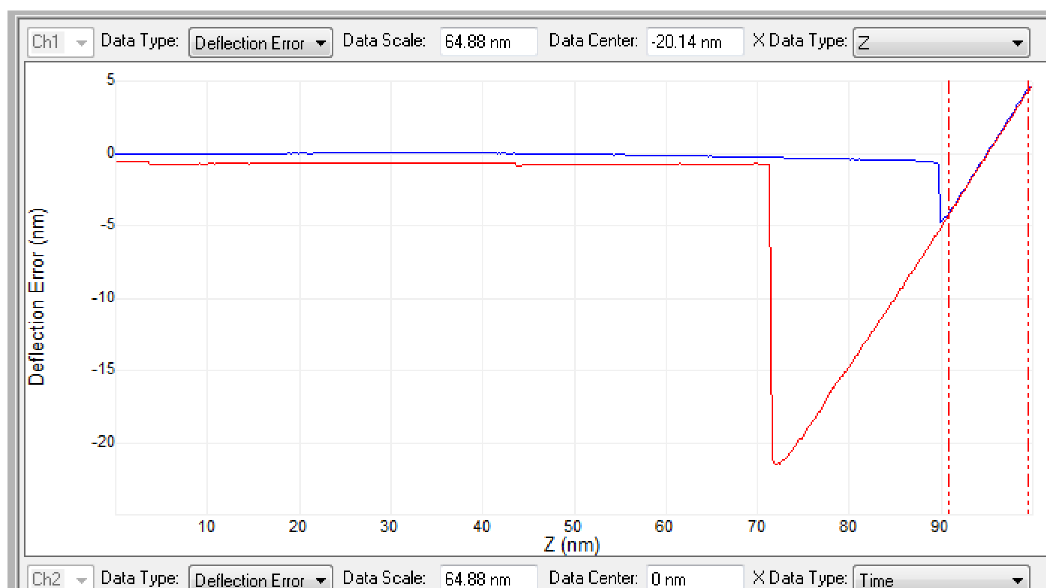

Figure 33. Deflection vs. Z plot.

11. By clicking **Update Sensitivity** the software will automatically calculate the deflection sensitivity and open the Set Realtime Channel Sensitivities window. By pressing **Ok**, the user enters the calculated value of **Deflection Sensitivity** parameter into the system.

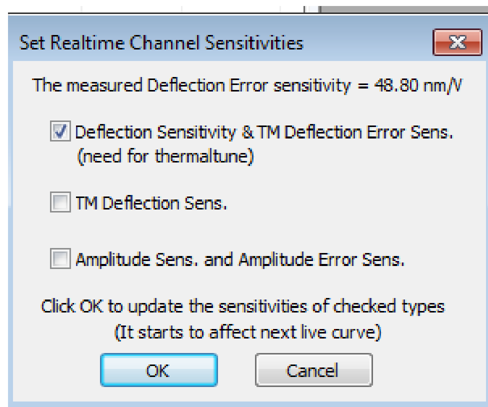

Figure 34. The Set Realtime Channel Sensitivities window.

12. Now it is possible to calibrate the **Peak Force Tapping Deflection Sensitivity**. To calculate the Peak Force Tapping Deflection Sensitivity press Update Sens bottom in the Force Monitor window, which is shown in Figure 35.

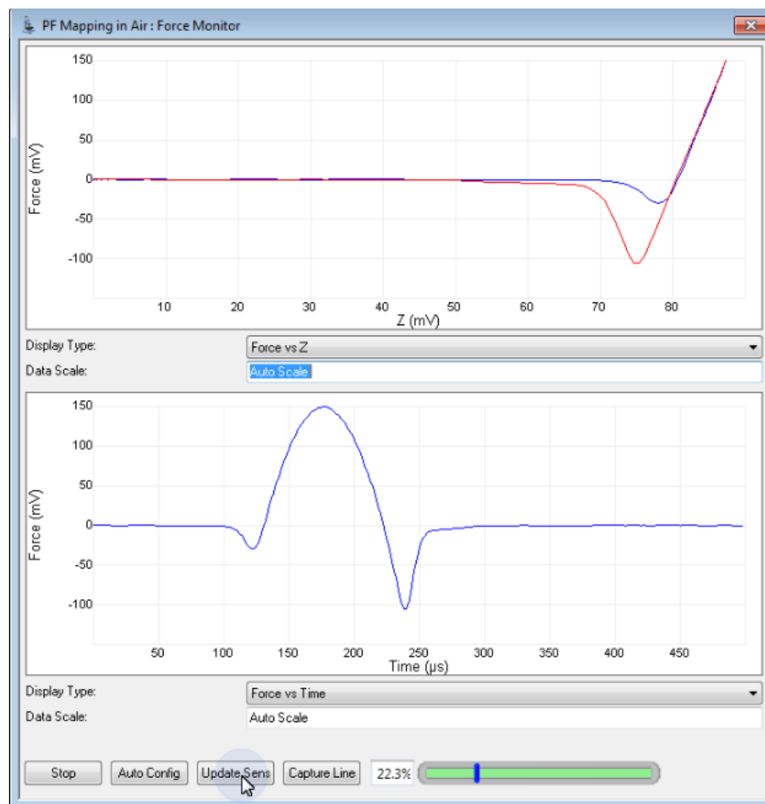

Figure 35. The Force Monitor window.

This opens the Set Sensitivity window (Figure 36). This function calculates the sensitivity of the cantilever deflection in Peak Force Tapping mode and compares it with the previously measured sensitivity of the Ramp Mode deflection sensitivity.

The deflection sensitivity should be equal for both modes.

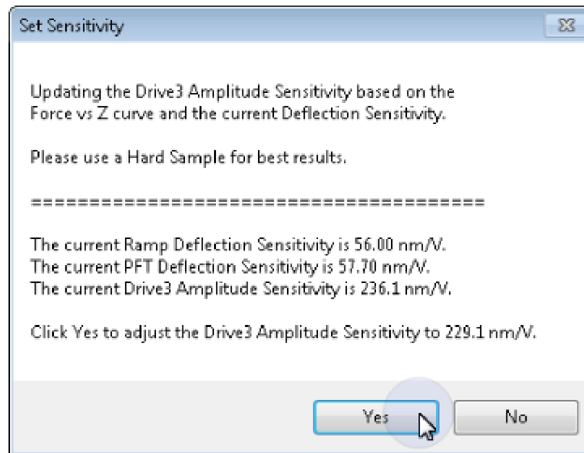

Figure 36. The Set Sensitivity window.

13. Before calibrating the **Spring Constant**, it is necessary to remove the probe from the sample surface. For this setting, it is important that there is no interaction between the probe and the sample. Calibration occurs in the **Thermal Tune** mode. The Thermal Tune Range is selected for each probe based on its characteristics specified by the manufacturer on the package. It is necessary to check the resonant frequency of the probe and select the range into which this frequency is included. For example, the PFTUNA probes have a resonant frequency of approximately 45 kHz and for it the Thermal Tune Range is 1-100 kHz, while for the LTESP probes with a resonance frequency of 150 kHz the range is 5-2000 kHz.

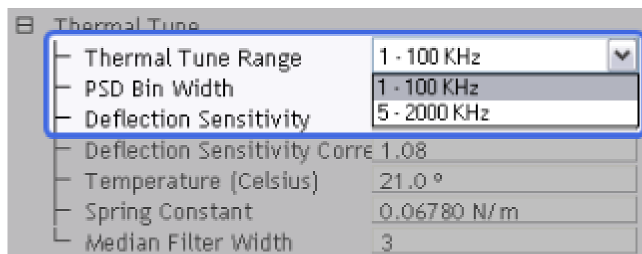

Figure 37. Select Thermal Tune Frequency Range.

Using the **Thermal Tune** panel, the Spring Constant is calculated.

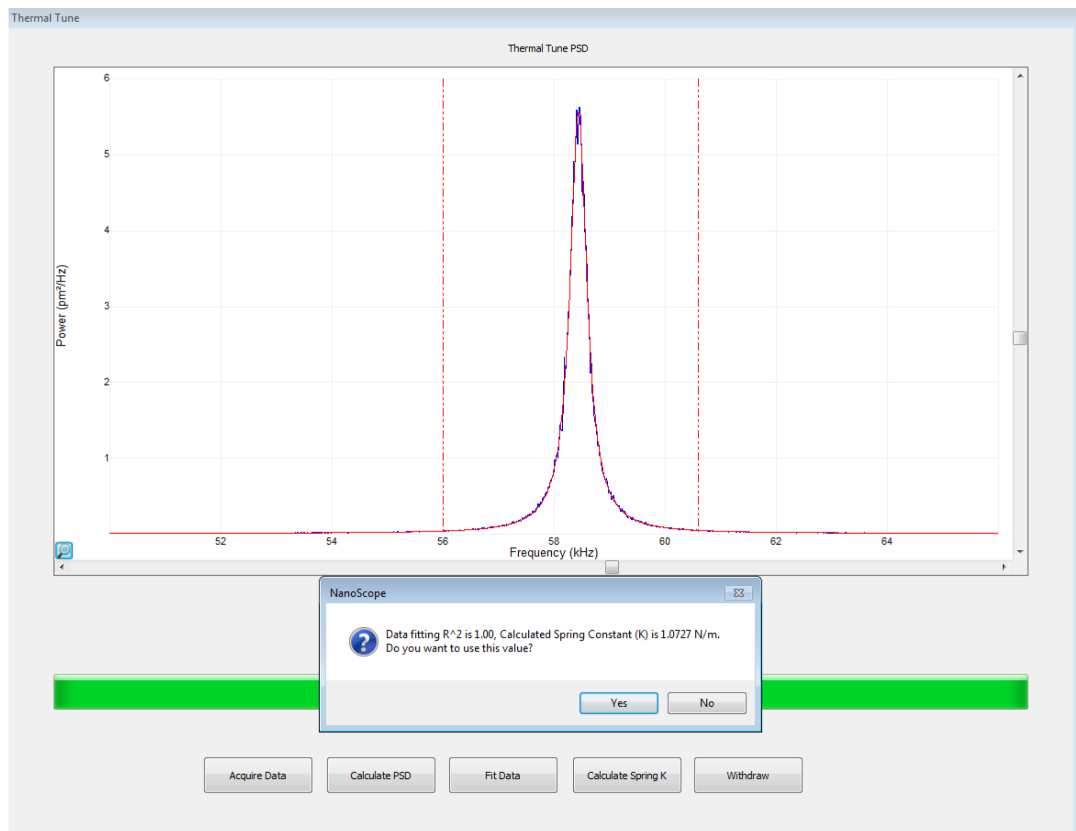

Figure 38. The Thermal Tune panel.

Taking the value of the stiffness constant calculated by the system, the operator will continue to work with this value.

Step 2 about 5 min. After the probe selected for operation has been calibrated, it is necessary to replace the reference sample with a test sample. In our case, this is a piece of silicon with gallium phosphide NWs, fixed to a metal substrate by a silver paste.

To measure mechanical properties by AFM bending, NWs that were individually standing and inclined at an angle of ~ 20 degrees to the substrate are the most optimal. Such requirements are predicated on the assumption that nearby objects did not affect the measurement process. In view of the existence of these requirements, before the measurement on the AFM the sample was placed in the SEM.

With the help of SEM, it is easy to find suitable NWs, and then to make a series of images at different magnifications, after which it is possible subsequently to find these NWs in an optical microscope. It's easy to orient on the sample's surface by using positions and orientations of scratching, dust or defects. Comparing the images of the SEM and the optical microscope, one can find the optimal area on which the NWs of interest are located. Figure 39 shows how to perform a series of images by SEM.

In Figure 39, suitable NWs for measurement are drawn in red, and noticeable objects around NWs in purple and green. With minimal magnification, it can be seen that the NWs are located in the lower right corner of the sample.

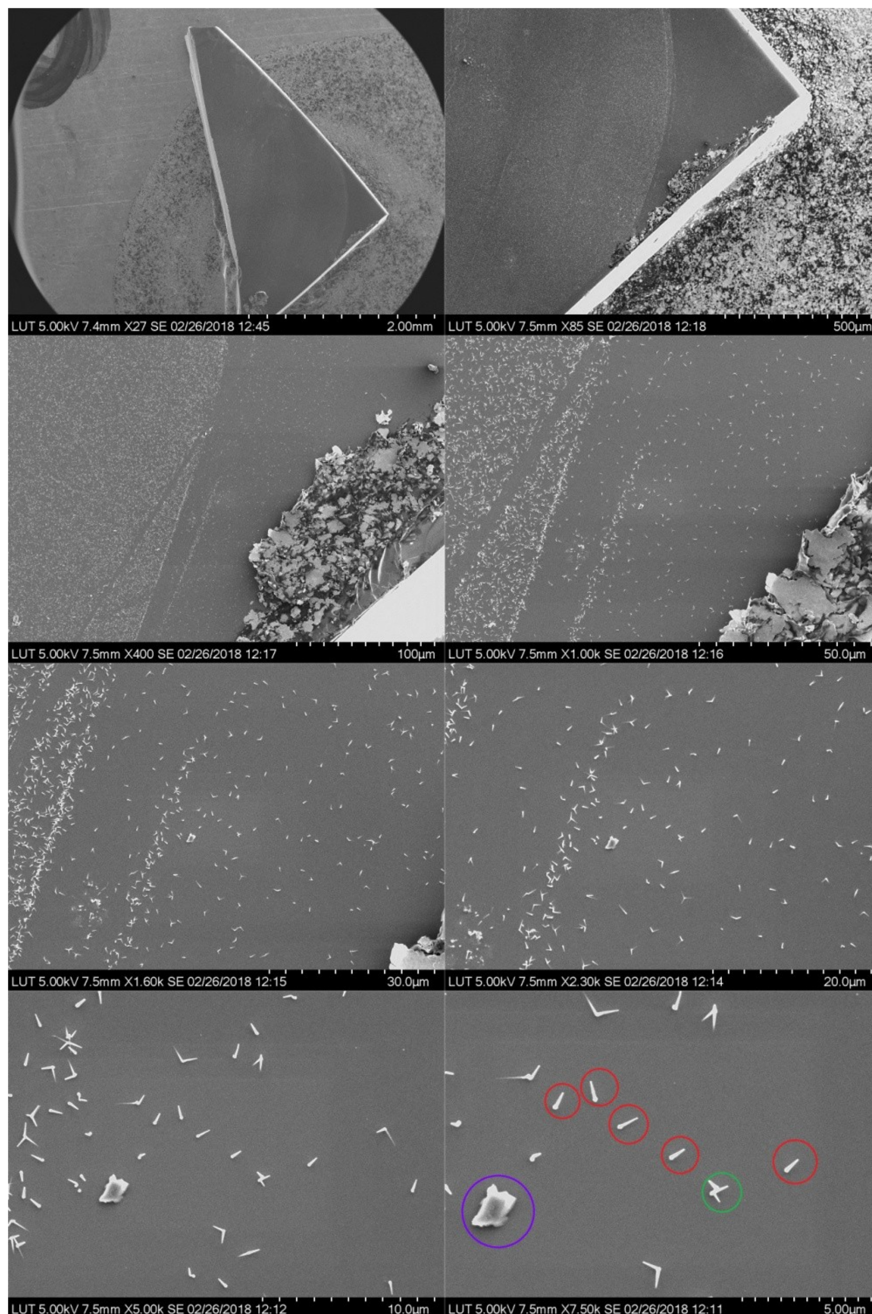

Figure 39. SEM images of the sample.

Putting a sample in an AFM in an optical microscope, one can observe the following shown in Figure 40. It can be seen that the position of the sample in the AFM differs from the position of the sample in the SEM chamber. However, this does not prevent to determine the angle in which the necessary NWs are located.

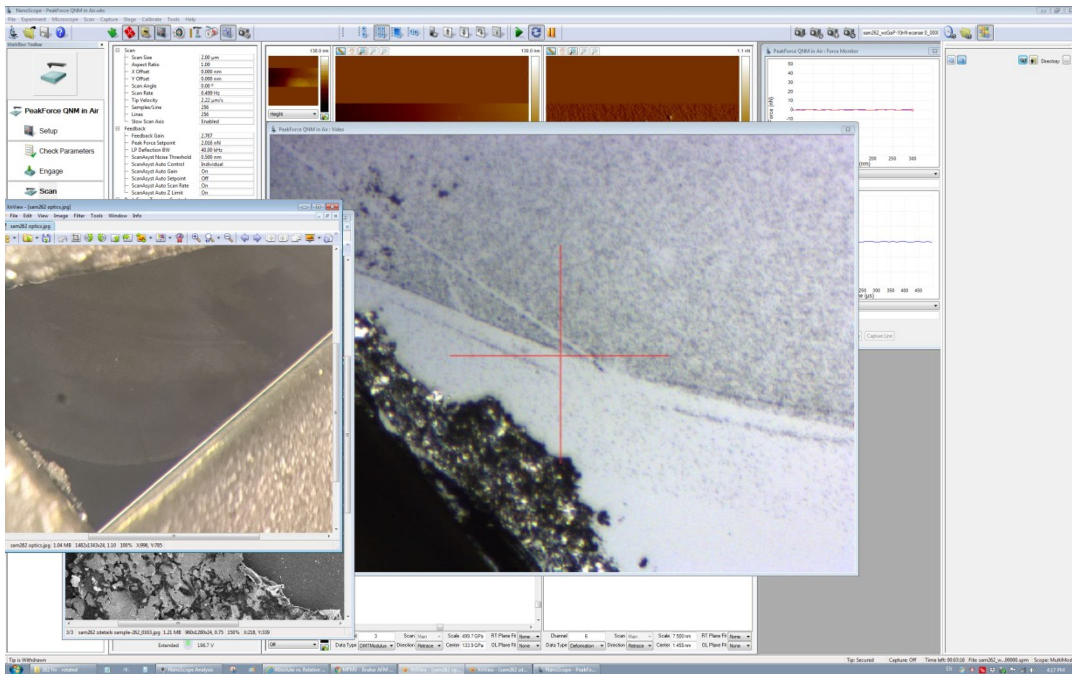

Figure 40. Window of the optical microscope of the AFM system opened in the software. To the left, for convenience, sample image is open.

After the AFM scan is completed, the following AFM images in Figure 41 are obtained.

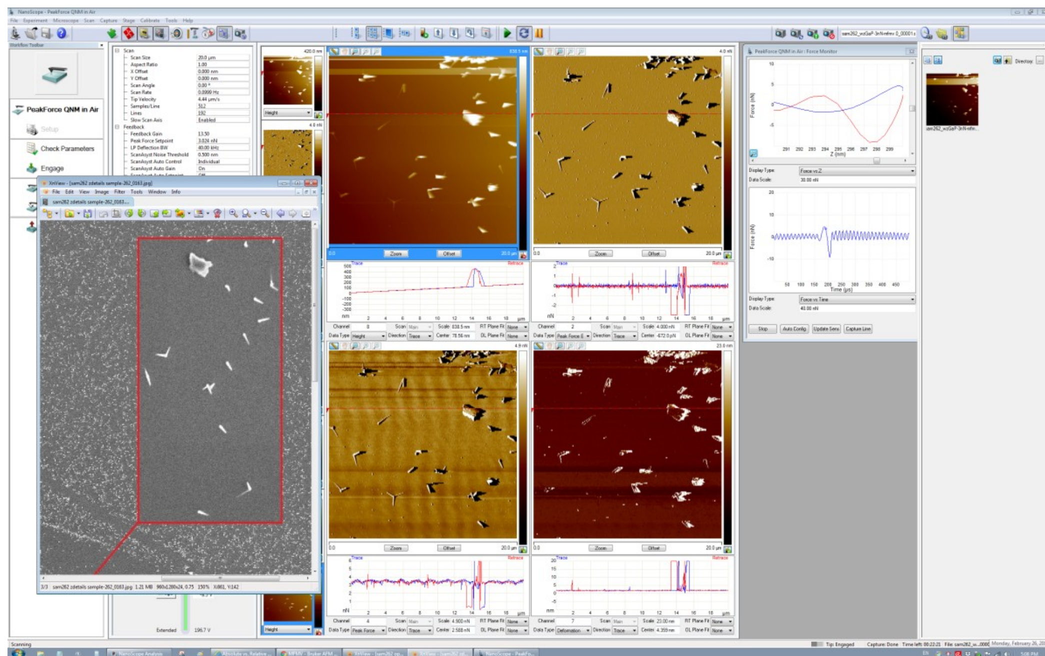

Figure 41. NanoScope program window contains data for channels Height (in Trace and Retrace), Deformation and PeakForce.

After a detailed comparison of the data obtained by AFM and SEM, it can be seen that the location of the NWs is quite accurate. Figure 39 shows a detailed comparison.

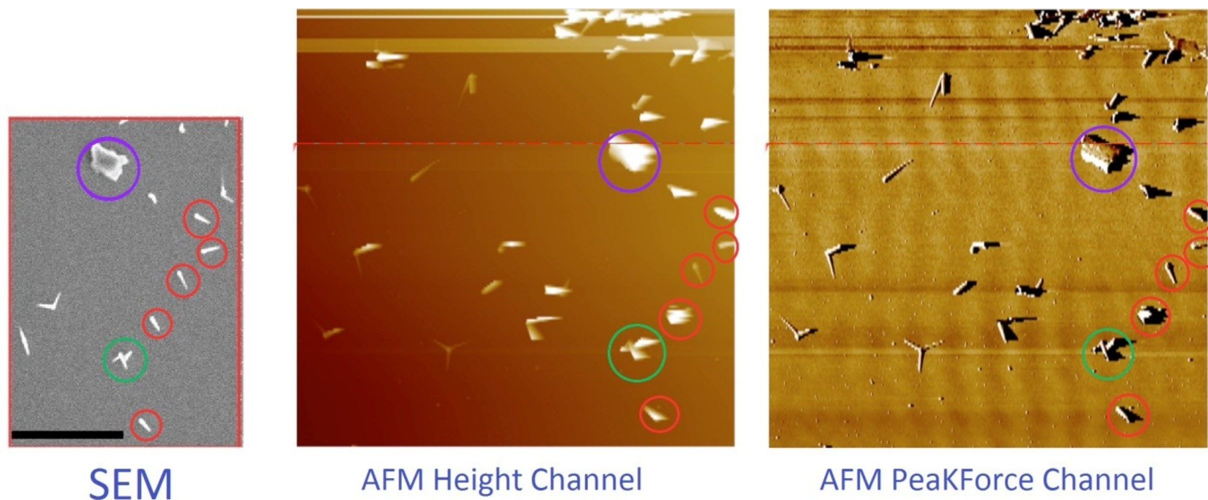

Figure 42. Comparison of the data obtained by AFM and SEM, scale bar: 5 μm.

This method saves time to find suitable NWs. As can be seen from Figure 42, the search can be performed with an accuracy of a few microns.

Step 3 about 45 min. It is necessary to pay attention to a step-by-step procedure for making measurements. As already mentioned, measurements will be performed in the PeakForce QNM mode. Engage the probe on the sample's surface. Start scanning from a small area (500 nm). Choose the number of scan lines (Samples / Line, Lines). Change the force of probe-sample interaction of the Peak Force Setpoint and the Z limit, if it is needed.

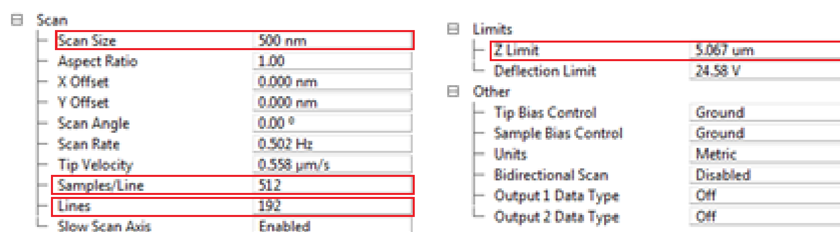

Figure 43. The first parameters to be changed at the beginning of the measurements.

To obtain the data necessary for the work, we need the channels **Height** (it both **Trace** and **Retrace**), **Deformation** and **PeakForce**. For **RT Plane Fit** and **OL Plane Fit** choose **None** in all channels. This is done in order to get raw data with the ability to independently change them in the future.

To find NWs, as described in the **Step 2**, it is necessary to scan a huge region of the sample (up to 20 μm). Since at this stage the resolution for us does not play a special role, firstly we will reduce the number of lines along the y axis to 128 – 256 lines, which will shorten the scanning duration. Decrease the strength of the PeakForce Setpoint to 2 – 5 nN (Optimal force, which allows just scan but not to crush the structure). Reducing the Scan Rate to 0.1 Hz is also

necessary to decrease the tip velocity and not destroy the NWs. Ensure that the Tip Velocity will not exceed 4 μm / s. Finally, increase the Scat Size to 20 μm.

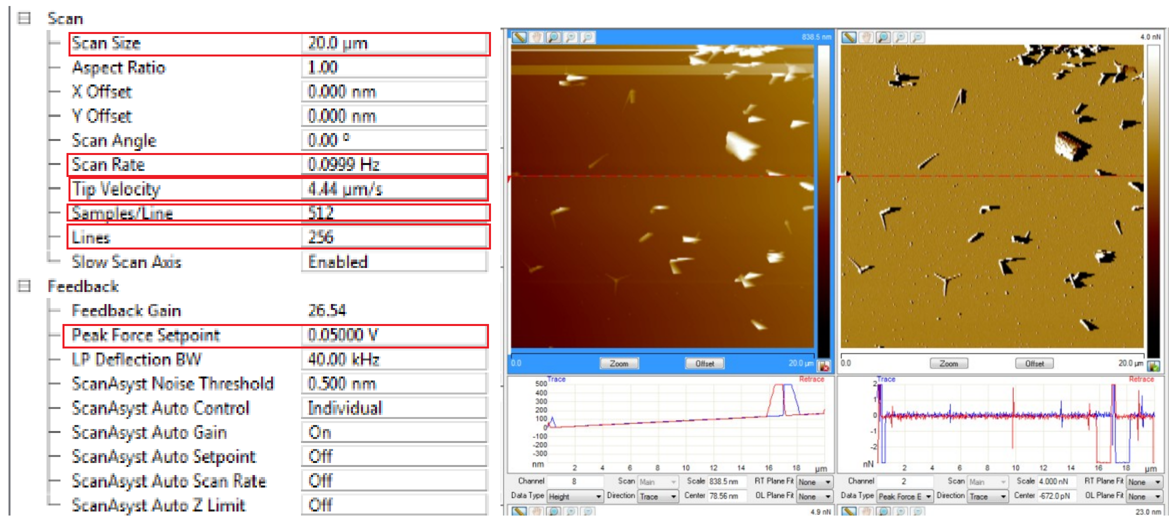

Figure 44. Scanning parameters and AFM image scan of 20 microns.

Scanning a field of 20 x 20 μm takes about an hour. If one need to get an exact value, it is possible use the formula:

$$Time = \frac{Lines}{ScanRate} \quad \textbf{(23)}$$

The scanning speed can also be calculated using the following formula:

$$V = \frac{S}{t} = ScanSize^2 \cdot ScanRate \quad \textbf{(24)}$$

For example, Tip Velocity and Scanning Time for scan with 512 lines and different Scan Size and Scan Rate are calculated in Table 2.

Table 2. Scanning Parameters.

Scan Size, μm	0.5	0.5	20	20
Scan Rate, Hz	1	0.1	0.1	1
Tip Velocity, μm/s	1	0.1	4	40
Time, min	8.5	85	85	8.5

Step 4 about 35 min. At this stage one has an AFM image of the scan area of 20 µm. Based on the distinctive features of the substrate, find the necessary NWs. Select one, place it in the center of the scan, and reduce the scan area.

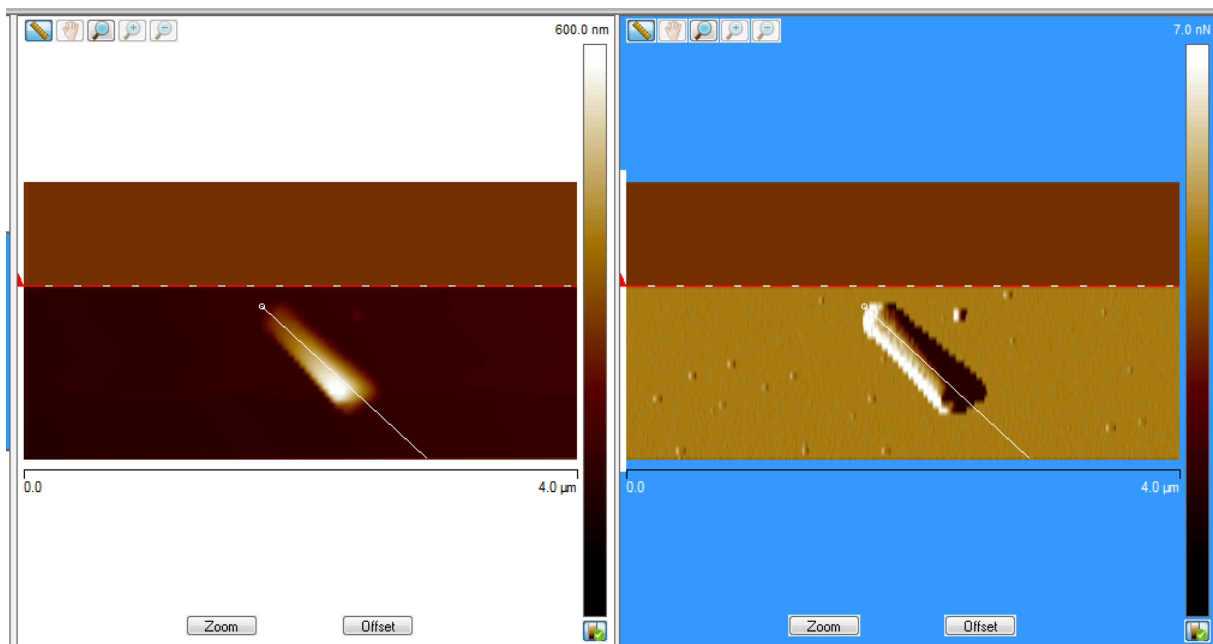

Figure 45. Single NW scanning on process, left is Height channel, right is PeakForce channel.

Expand the sample in such a way that the NW is placed parallel to the last scanning direction. NW should be oriented in such a way that the slope of the NW is compensated by the inclination of the AFM cantilever. Increase the Aspect Ratio, increase the number of lines for greater resolution.

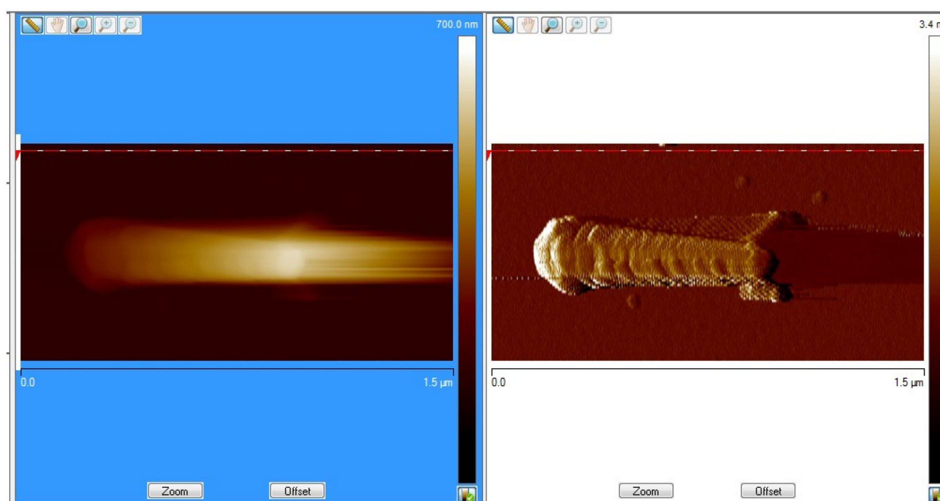

Figure 46. Single NW scanning on process, the angle of scanning was changed, left is Height channel, right is PeakForce channel.

All scans must be made in one scanning direction (select Up or Down). At the beginning of each new scan, operator need to adjust the moment of PeakForce curve calculation using the Auto Config, which is displayed in the changes to the Sync Distance parameter.

Change the Peak Force Setpoint to investigate the mechanical properties of the NW. When working with an individual NW, it is needed to obtain as much detailed data as possible. To do this, it is necessary that the width of one scan line is much smaller than the diameter of the NW. To calculate the line width by dividing the scan height value to the number of lines. The width of the scan is specified by the operator (Scan Size), the height is calculated from the aspect ratio (Aspect Ratio).

Thus, after completing Steps 1-4, the output gives AFM data on Height, Deformation and PeakForce for an individual standing NW, measured with different values of the PeakForce.

Parameters that introduce an insignificant error in AFM measurements:

1. Feedback Noises or Device noises. For example, noise on the photodetector – the laser spot on the photodetector changes its position at a speed greater than the system can reproduce. Such noise makes an error of about 50 pm.

2. ScanAsyst Noise Threshold value.

3. Changing the tip apex shape during measurement.

4. PeakForce Setpoint value.

5. Air, acoustic, mechanical vibrations.

6. Software Segmentation (Quantization) on Z-Limit.

All of the above parameters make an insignificant contribution to the error, about a dozen picometers. The greatest contribution to the calculation error is made by the following parameters, which are not necessarily related to the features of the AFM operation:

1. The difficulty in determining the exact value of R_{mid} and D_{mid} for NWs. Determining the diameter and radius of the NW with high accuracy using SEM can be difficult, since NWs have a diameter on the order of several dozens of nanometers and a deviation of only a few nanometers will significantly change the calculation result.

2. Scatter in the values of PeakForce.

3. The work in the NanoScope Analysis program will be described in chapter 3.3., However, work in this program can both improve the result of calculations, and significantly degrade it. In this program, we take out the Heights and PeakForce profiles to further calculate

the Young's modulus. However, the line on the AFM image of the NW, from which the profile will be taken out, can vary from scan to scan. I.e. there can be a situation that for comparison different points will be taken on the NW, which will lead to an increase in the error magnitude.

4. The point of attachment of the NW to the substrate. Since in AFM and SEM only the top view of the NW is visible, it is difficult to say how it is fixed to the substrate and what percentage of its length constitutes the fastener. The point of attachment of the NW to the substrate in the literature is called the NW base.

3.3. Experimental data processing

To process the data received on the AFM, the following programs were used: NanoScope Analysis 1.8 and Origin 8. First, the experimental data is opened in the program NanoScope Analysis 1.8. This program allows to obtain deflections profiles of NWs, as well as profiles of force applied along the length of the NW. Deformation Profile yields data on the quality of the measurements. If a deflection is observed along the length of the NW in the deformation channel, then it is probable that the NWs were able to bend qualitatively.

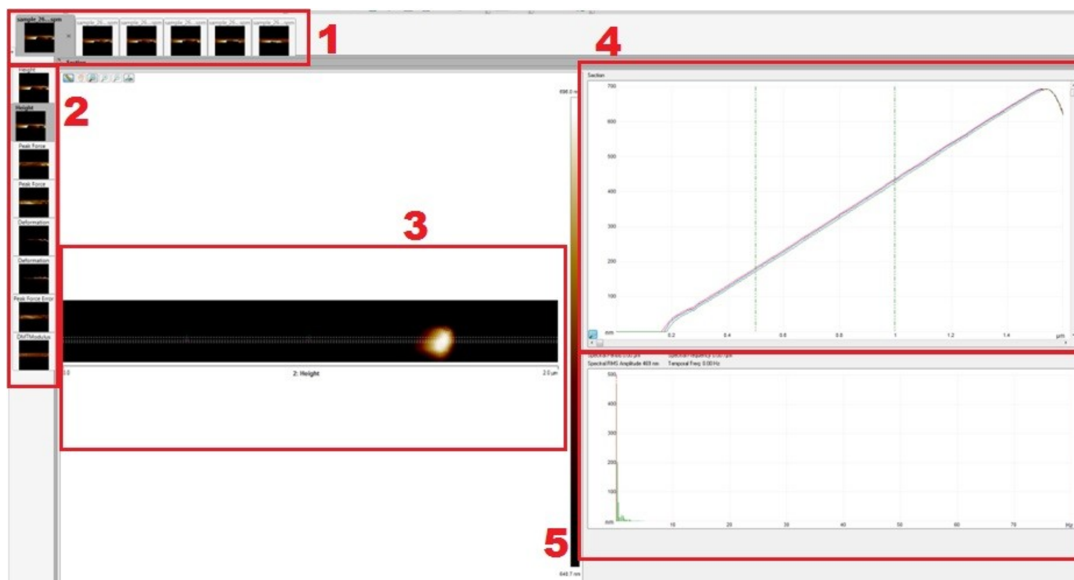

Figure 47. Obtaining the height profile of a NW in the NanoScope Analysis 1.8 program, channel Height.

Figures 47-49 show the NanoScope Analysis windows. Figure 47 contains the following parts: the scan tabs (1), the scanned channels (2), scan image (3), the profile or section obtained from the line selected on the scan (4), and the distribution graph according to the channel (5). Figures 48-49 contain the same parts, but for the Deformation and PeakForceI channels, respectively.

Any profiles, containing data on NWs, are best obtained throughout their length: from the beginning of growth on the substrate to the free edge of the NW. On the scan, it is possible to determine the free end of the NW, this is the highest point on the scan.

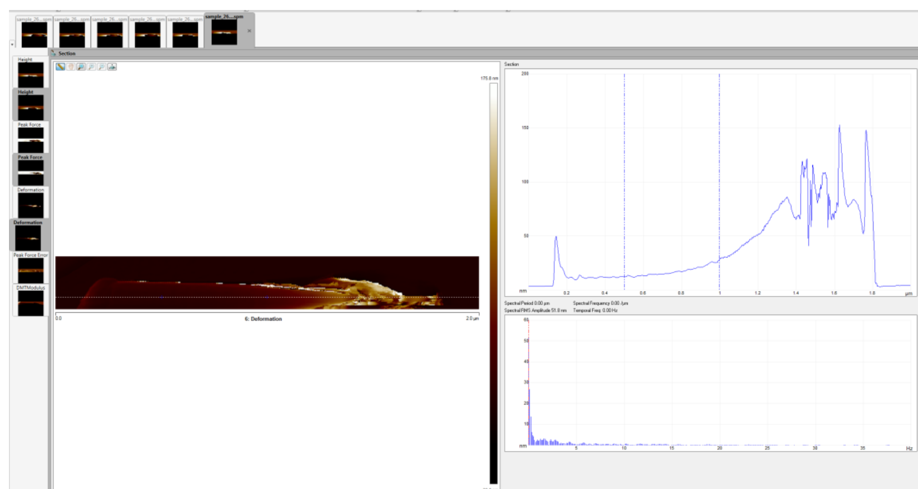

Figure 48. Obtaining the deformation profile of a NW in the NanoScope Analysis 1.8 program, channel Deformation.

Similarly, obtain data on the deformation profile and the forces from the channels Deformation and PeakForce, respectively.

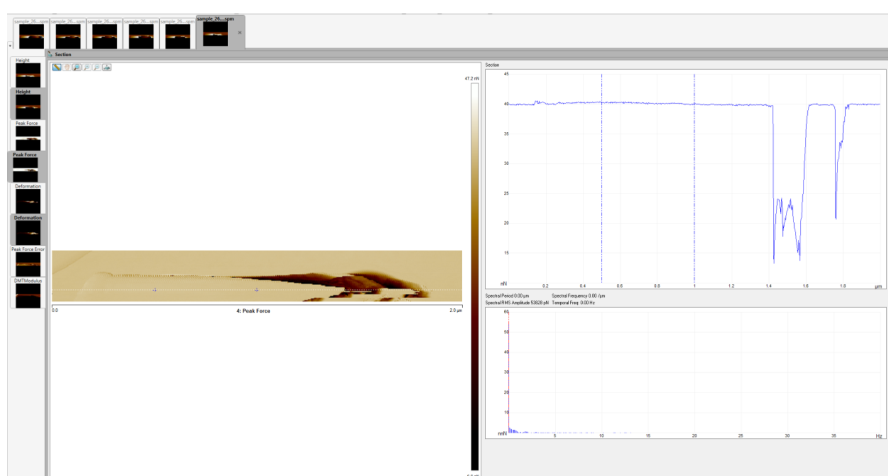

Figure 49. Obtaining the force profile of a NW in the NanoScope Analysis 1.8 program, channel PeakForce.

As can be seen from Figure 47, the NW is indeed located at an angle of about 20 degrees to the substrate. In accordance with [75-76], NWs of compounds III-V, grown by the MOVPE method on Si (111), experience four main directions of crystal growth. According to the crystallography rules, for a crystal plane with orientation (111), four equivalent directions are distinguished: one orientation perpendicular to the surface and three orientations having a 19°

angle with the surface and having in-plane components at an angle of 120° from each other, as shown in Figure 50.

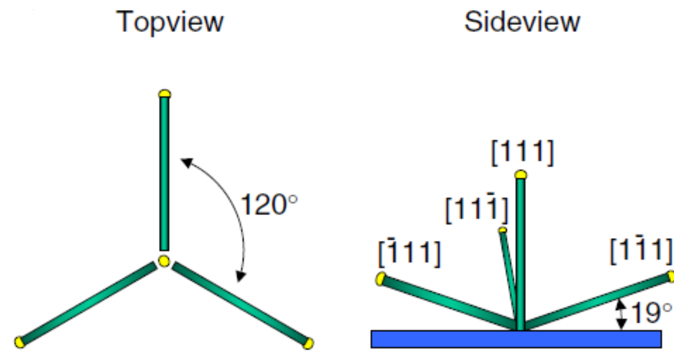

Figure 50. The threefold symmetry of wires grown in the [111] direction on a (111) surface can be clearly seen. Wires grown perpendicular to the (111) surface can be seen as dots. (a) A schematic top view and (b) a side view to illustrate the four [111] directions in which the wires grow [75-76].

In directions with negative Miller indices, inclined NWs with an angle to the substrate of 19-20° are formed. The angle of inclination can vary due to unevenness of the surface, defects, etc. In this work, for ease of calculation, the angle of inclination was assumed to be ~20 degrees.

4. RESULTS AND DISCUSSION

In this chapter, the results of measurements and calculations will be discussed and compared with results of other authors. Also, in 4.2., recommendations for improving the experiment are given.

4.1. Experimental results

During the experiment, forces magnitudes of 1, 2, 5, 10, 20 and 40 nN were applied to the individual standing inclined NWs.

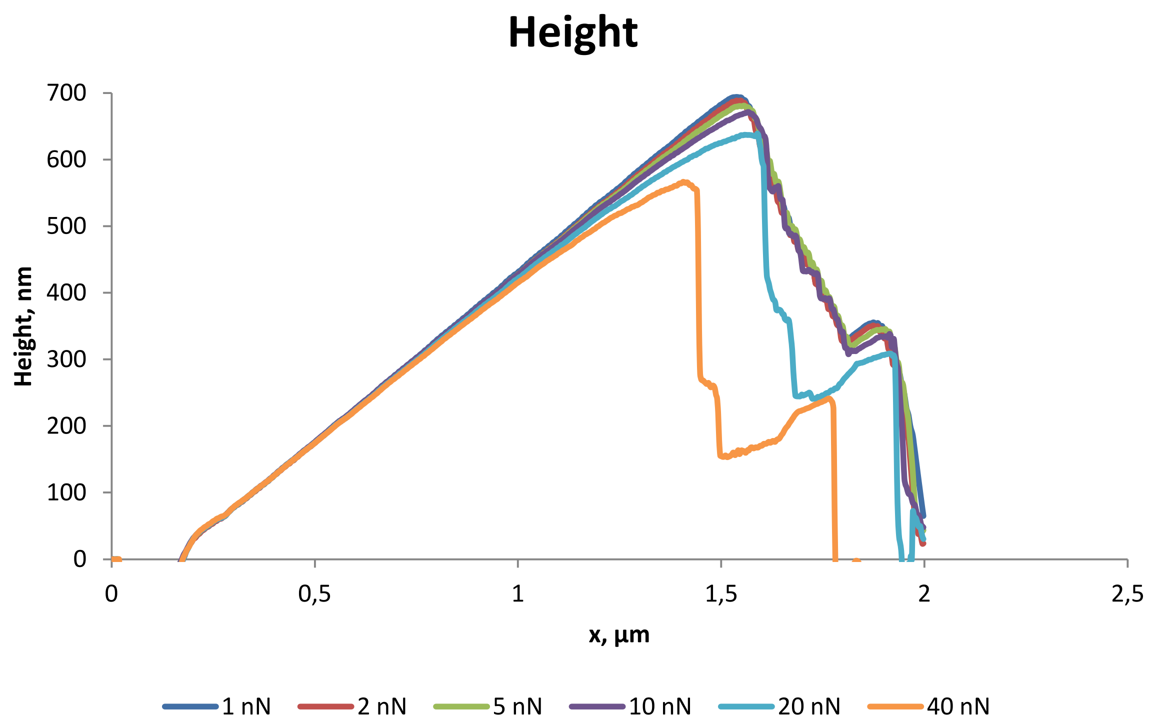

Figure 51. The height profiles of the NW obtained with different peak forces.

Figure 51 shows the height profiles of the NW obtained with different forces of the AFM cantilever pressing. From this graph it can be seen that when a greater force is applied, the wire bends more strongly, which is to be expected. This and all subsequent graphs will show not the absolute height, but the relative with respect to the height of the NW obtained at a force of 1 nN. Having removed the data not used for calculations, we will receive the following profiles as shown in Figure 52.

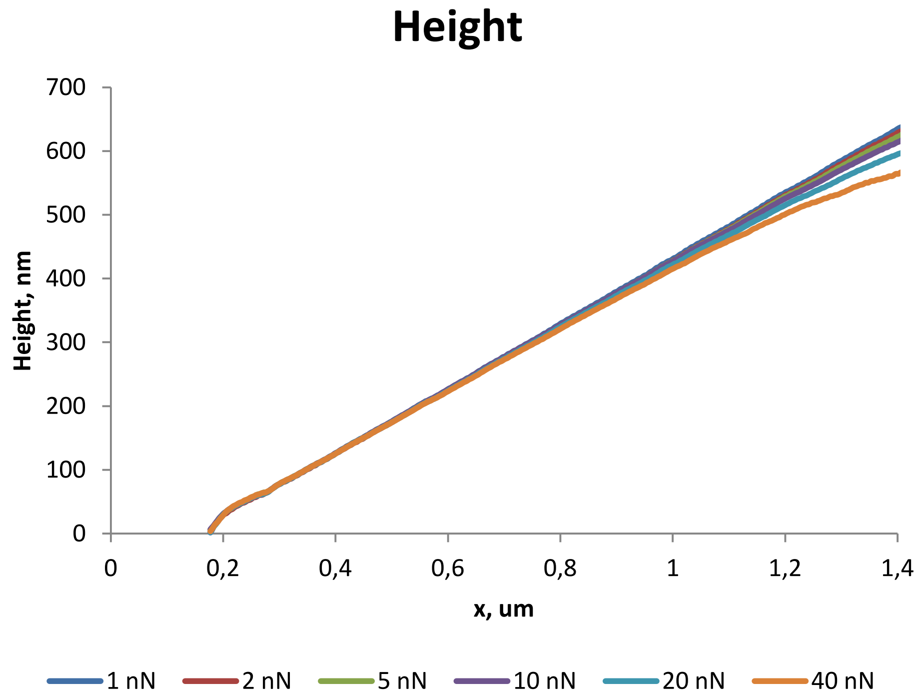

Figure 52. The height profiles of the NW obtained with different peak forces, the profile is selected along the length of the NW.

Conditionally, we assume that when measuring a NW with a 1 nN force the bending was absent. That is, the bending for the force 1 nN is zero. Next, it is necessary to calculate how strongly the NW has bent under the application of large forces. To do this, it is necessary to take the heights of the NW, obtained with other forces, one by one from the height value at a force of 1 nN.

Thus, the bending value can be calculated from the formula:

$$Bending(F_i, nm) = Height(F = 1nN) - Height(F_i) \quad \textbf{(25)}$$

Where:

Bending(Fi, nm) is bending value, when applying force *Fi*= 2…40 nN;

Height(F = 1nN) is height of the NW, when applying the force *F* = 1 nN;

Height(Fi) is height of the NW, when applying the force *Fi* = 2…40 nN.

Bending profiles of the NW are presented in Figure 53.

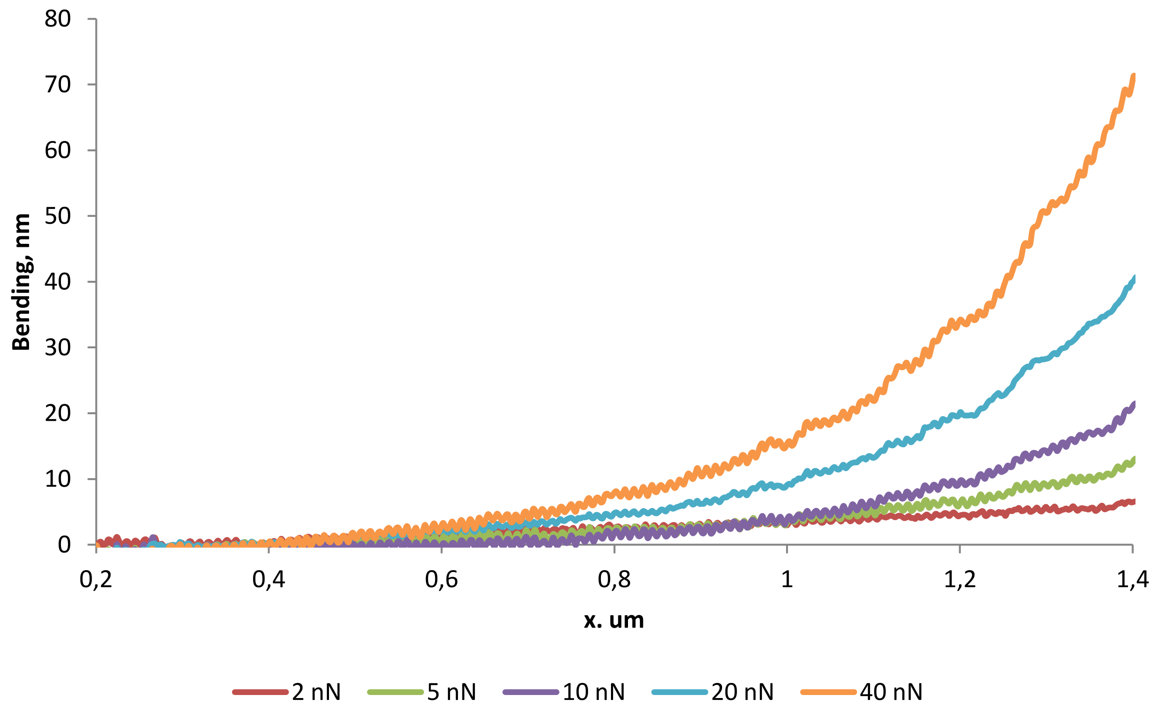

Figure 53. Bending profiles for various values of peak force.

Further, it is necessary to calculate the coefficient of flexibility f using formula **(21)** given in Chapter 2.3.

$$k = \frac{1}{f} = \frac{F}{w_{NW,F(x)}}$$

In accordance with this formula, we need to divide the bending value by PeakForce at which this bending occurred. As a result, we obtain curves of the flexibility profile for different forces as shown in Figure 54.

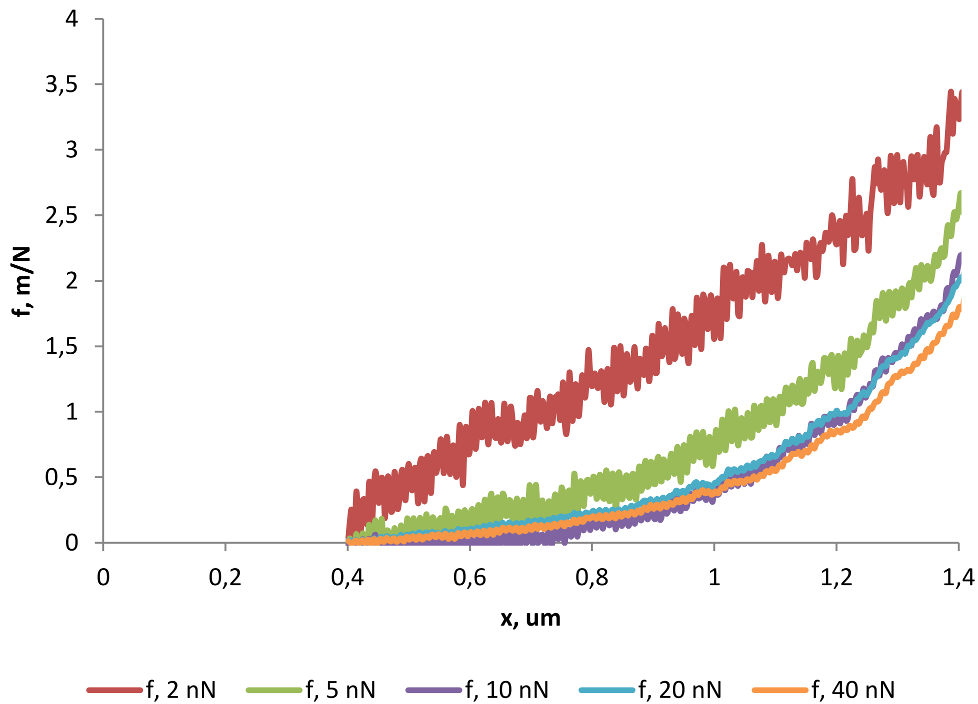

Figure 54. Flexibility profiles for various values of peak force.

As can be seen from Figure 54, the curve for a force of 2 nN has a linear form, in contrast to all the others. Such strong deviation may occur due to the reasons listed in Chapter 3.2. Also, this curve is obtained with a force that is not much different from the force taken zero-force. That is, since it is assumed that when the force of pressing 1 nN the NW is not deflected, then the deflection may be insignificant at a force of 2 nN, which leads to an error in calculating the coefficient of flexibility. Summarizing these factors, we will not take into account this 2 nN curve for further calculations.

Flexibility profiles were averaged resulting in a single curve for the flexibility coefficient shown in Figure 55. Further, this curve is loaded into the Origin program in order to be analyzed by a fitting function according to formulas **(23)** and **(24)** from Chapter 2.3**.**

$$f(x) = \frac{1}{k(x)} = \frac{64}{3\pi}\frac{1}{E}\frac{1}{D_{mid}^4}\frac{x^3}{(1+a_1(2x-L))(1-a_1L)^3} \qquad \textbf{(23)}$$

and:

$$\mathrm{E} = \frac{64}{3\pi}\frac{1}{f(x)}\frac{1}{D_{mid}^4}\frac{x^3}{(1+a_1(2x-L))(1-a_1L)^3}. \qquad \textbf{(24)}$$

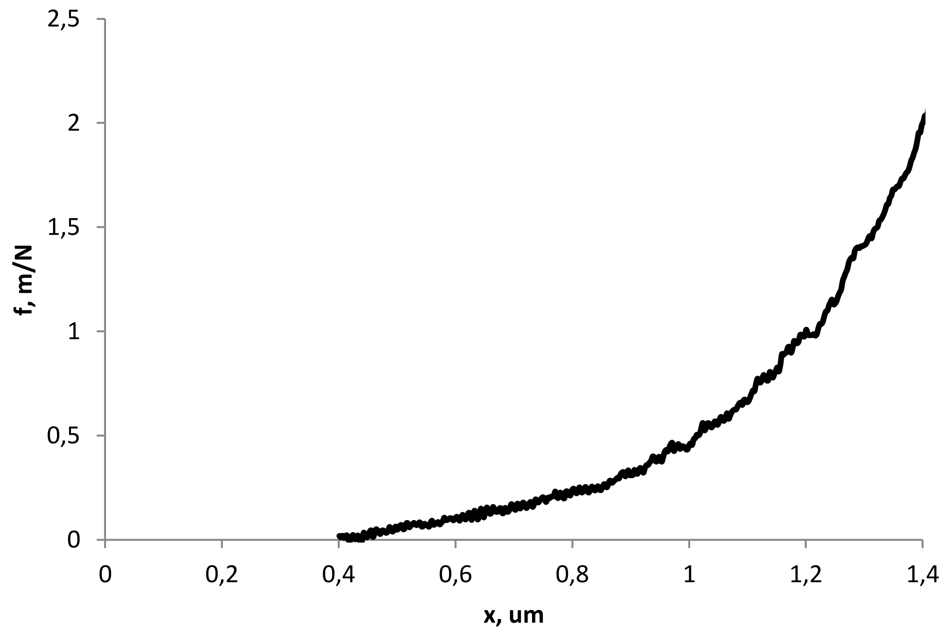

Figure 55. Flexibility profile of NW, averaged curve.

Thus, a flexible profile is applied as an input, and flexibility coefficient curve is fitted according to the formula (25):

$$f(\mathrm{x}) = \frac{b(x-x_0)^3}{(1+a_1(2x-2_0-L))(1-aL)^3} \quad \textbf{(25)}$$

where $b = \frac{64}{3\pi}\frac{1}{E}\frac{1}{D_{mid}^4}$ and $a_1 = \frac{\alpha}{D_{mid}}$.

The fitting function was created by Mikhail Dunaevsky and is described in more details in works [66, 71].

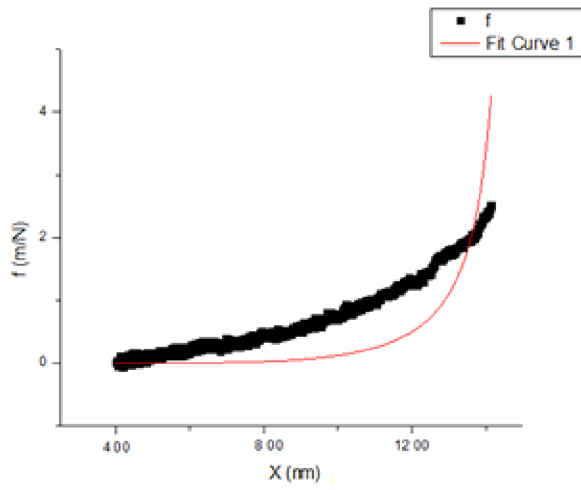

a)

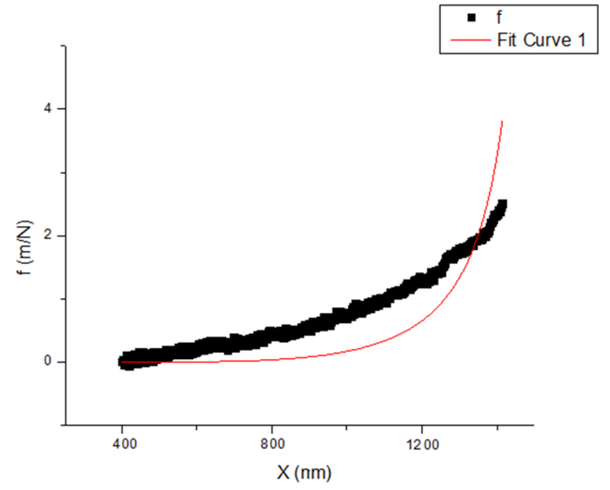

b)

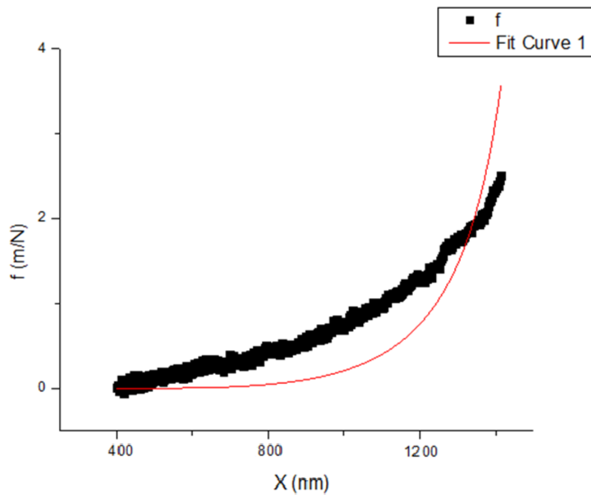

c)

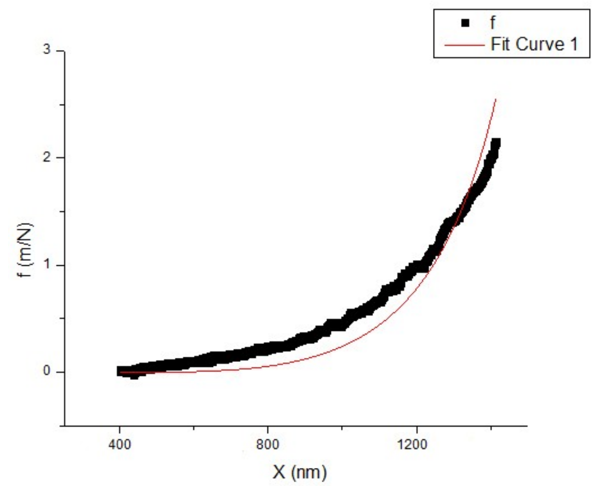

d)

Figure 56. Flexibility profile of NW, averaged curve (black) and Fitting curve (Red): a) D_{mid}=60 nm; b) D_{mid}=65 nm; c) D_{mid}=70 nm; d) D_{mid}=90 nm.

In Chapter 3.2., it was indicated that inaccuracy in measuring the diameter of the NWs leads to huge errors in the Young's modulus calculations. Table 3 shows the calculations for different diameters. As can be seen from Table 3, the most significant parameter in determining the Young's modulus for NWs is the value of the median diameter of the NW.

For the calculations, the following value of a_1 was used:

$$a_1 = \frac{\alpha}{D_{mid}} = -\left(\frac{3^{\circ}}{D_{mid}}\right) = -\left(\frac{0.0523}{D_{mid}}\right)$$

Table 3. Results of Young's modulus calculations.

D_{mid}, nm	60	65	70	75	80	85	90
$-a_1*10^5$	8,717	8,046	7,471	6,973	6,537	6,153	5,811
E, GPa	199	114,6	76,6	55,2	41,5	32,2	25,6

4.2. Analysis of experimental results

As was demonstrated in chapter 4.1, when calculating the Young's modulus, based on the data obtained by QNM, the sensitivity of the method is high.

Figure 57 shows the dependence of Young's modulus on the D_{mid} of the NW, based on Table 3 data, if one put different D_{mid} into modeling, but not based on experimental results like in [66]. The parameters to be determined depend very much on the D_{mid}, and in combination with the uncertainty of other parameters it is only possible to estimate the value of the Young's modulus and it is approximately equal E=114.6 GPa when Dmid = 65 nm. For accurate determination of E, it is needed to measure D_{mid} with large resolution equipment. For example, for this problem high resolution SEM imaging or measurement of laying NW by AFM are suitable.

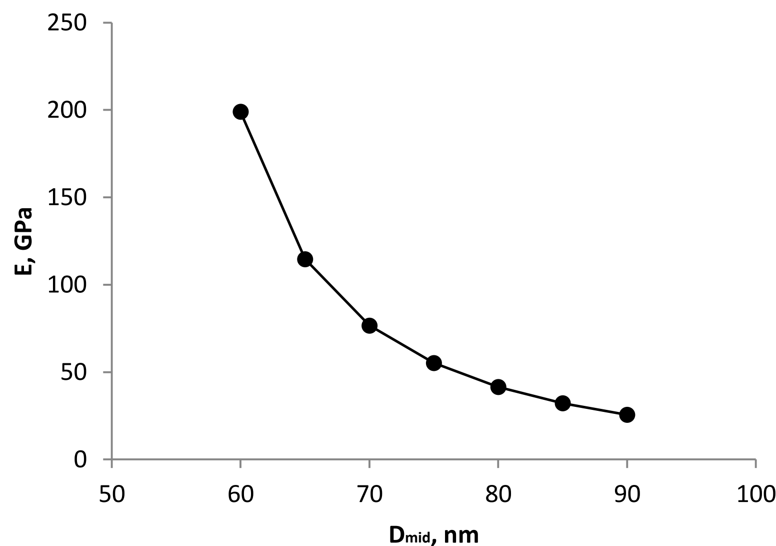

Figure 57. The variation of Young's modulus value, arising in this theoretical model due to the impossibility of accurate determination of the D_{mid}.

Figure 57 represents the scatter of the Young's modulus values due to the uncertainty of the diameter in the model, and not the value of the elasticity itself. The graph shows how

strongly the determination of the value of the D_{mid} affects the value of E in such model. As can be seen from Figure 57, Young's modulus value calculated in accordance with model varies greatly depending on the choice of the D_{mid} of the NW. The Young's modulus varies within the range of 25-199 GPa for the D_{mid} within 90-60 nm, respectively. Since experimental data on the measurement of the Young's modulus from other authors have not yet been obtained, these values can only be compared with those theoretically predicable in the literature. In works [77-78] plane-wave pseudopotential calculations were used for the study of elastic properties. Based on the data indicated by M.Sc. Pavel Geydt, the theoretically possible Young's modulus was calculated for GaP NWs it amounted to 179.4 GPa. It cannot be denied that many factors introduce an error in the calculation of the Young's modulus in the case of NWs. Next will be considered how it is possible to reduce the error value.

4.3. Prospects for the experiment

The following actions can be taken to improve the experiment of GaP NWs bending and to reduce the error in calculations of the Young's modulus.

1. AFM cantilevers modification

When studying the mechanical properties of NWs with the AFM method, the following problem arises: when the probe passes through the surface of the NW, instead of bending under the probe pressure it is laterally deflected.

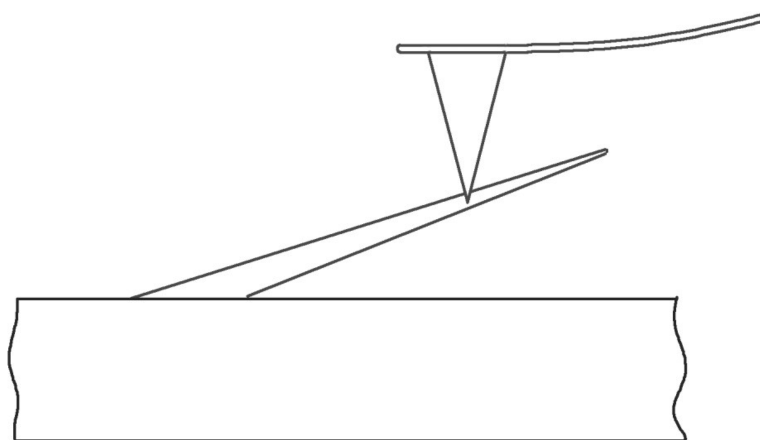

Figure 58. The way of NW investigation by means of AFM.

To solve this problem, it was suggested to modify the existing probes as follows: it is necessary to make a groove in form of a semicircle at cantilever's tip. Tip of such shape will

allow holding NWs under the pressure of the probe without lateral deviations. Figure 59 shows the principle of work of modified cantilever.

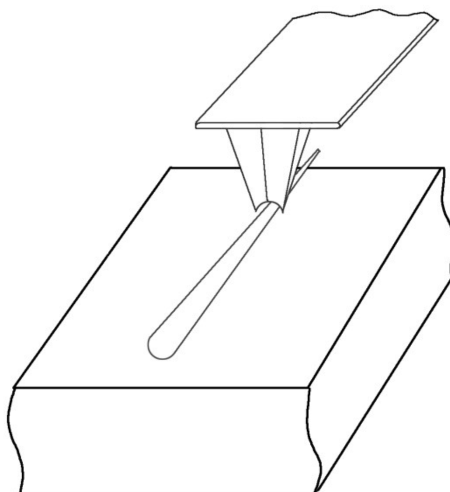

Figure 59. The way of NW investigation by means of AFM with modified cantilever.

To create a groove in the probe, it was suggested to use the FIB method. Based on the SEM data, it was found that the diameter of the NWs of interest varies from 10 to 180 nm. Thus, the distance between the edges of the modified probes was chosen to be within 150 nm.

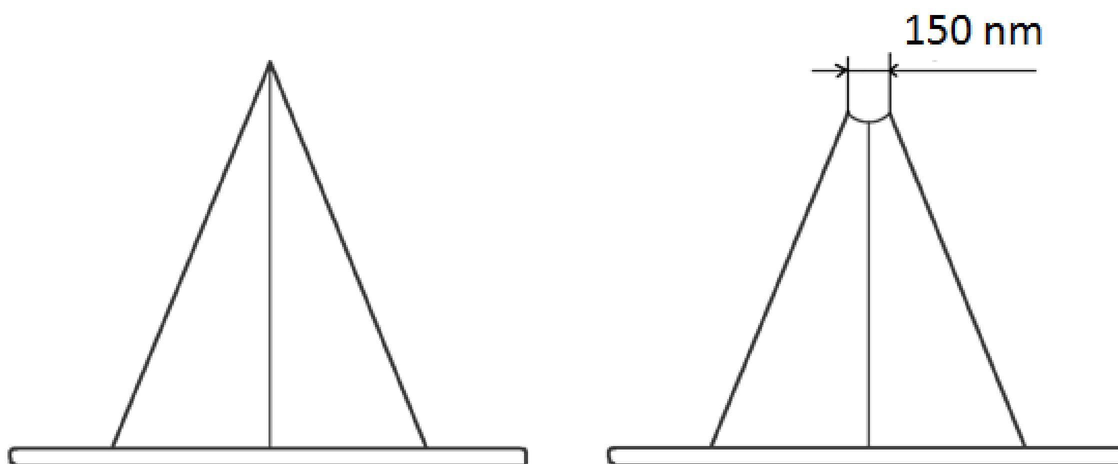

Figure 60. Schematic front view of cantilevers. Desirable shape of the tip.

The experiment was carried out on the Tescan Lyra3 microscope. The cantilevers were fixed on the conductive tape in such a way that the tip of the probe was located in front of the nozzle of the ion column.

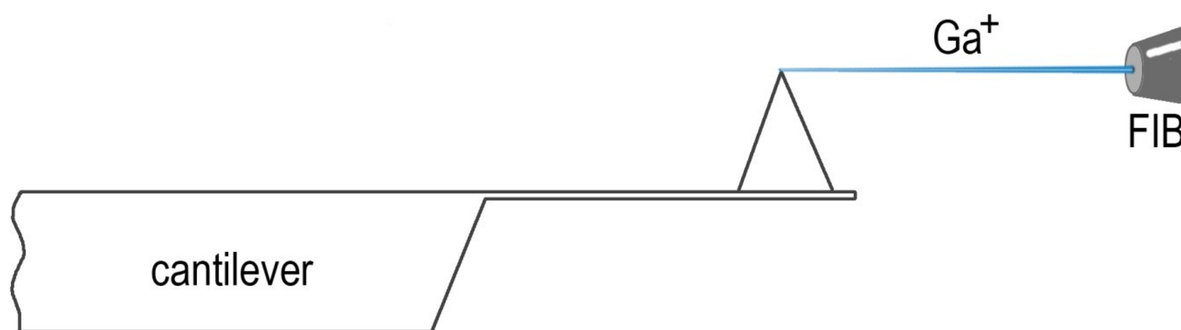

Figure 61. The way of the probe etching via FIB.

Bruker Scanasyst AIR and Bruker Scanasyst PIT were used as initial probes. As a result of the experiment, two modified probes were obtained. The final result is demonstrated at Figure 62.

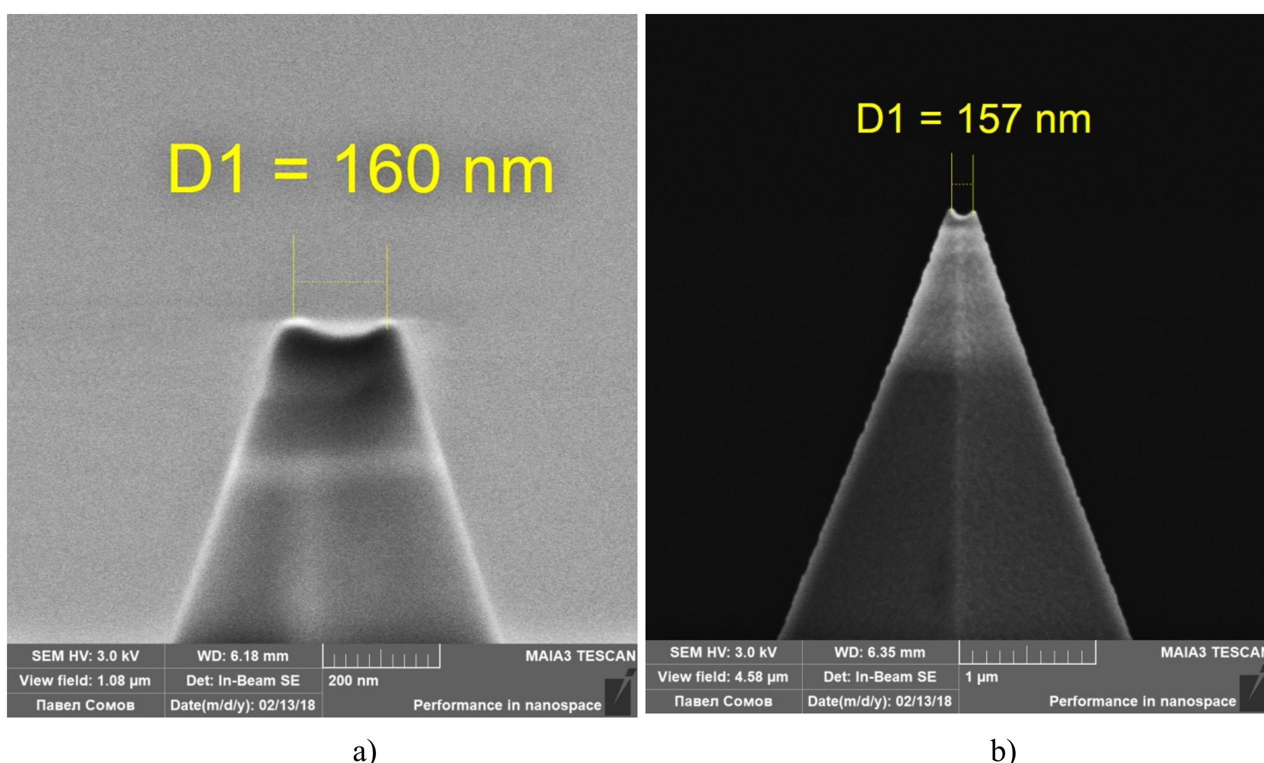

a) b)

Figure 62. Front view of modified cantilevers a) Bruker Scanasyst AIR, b) Bruker Scanasyst PIT.

2. Double-bonded nanowire structure

To study the mechanical characteristics of NWs, it would be useful to compare the results for calculated Young's modulus for NWs freely grown on a substrate (single- clamped NWs) and for a double-clamped structure. To obtain a double-bonded structure, it is necessary to etch the groove in monocrystalline silicon and, using a nanomanipulator, to deposit a NW over the groove, previously separated it from the substrate.

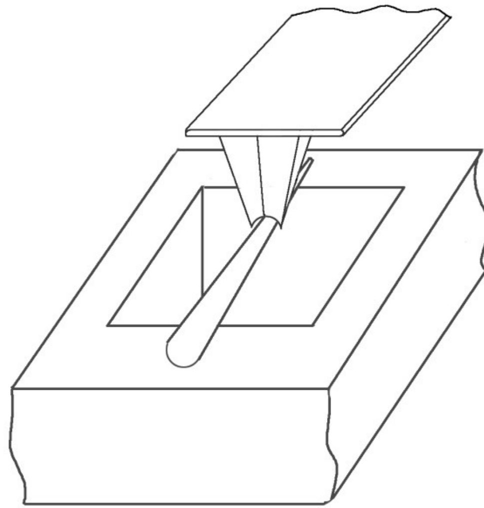

Figure 63. Double-bonded NW structure.

Figures 64-65 present the real experiment, which was held for InP NWs. Due to NWs size it isn't possible to create such structure as described above due to the diameter of InP NWs.

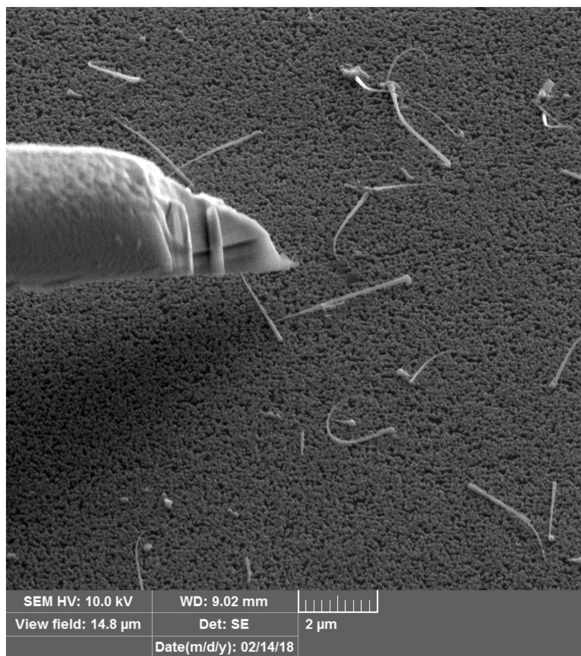

a)

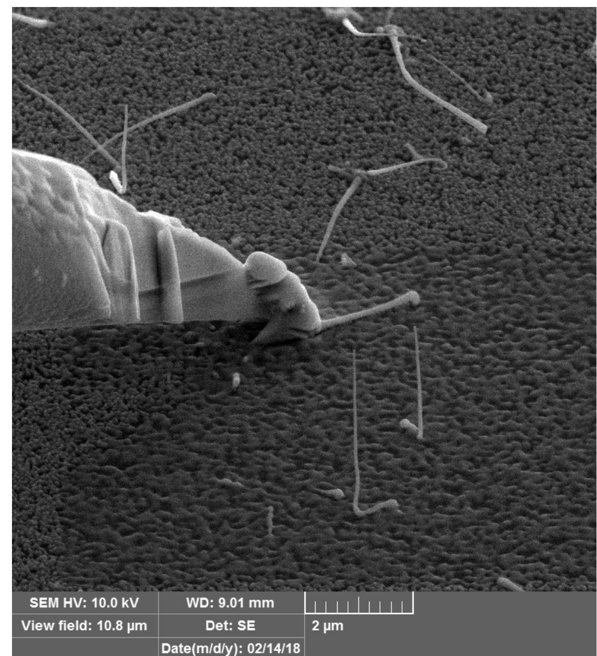

b)

Figure 64. a) The needle of the nanomanipulator (on the left) is already sharpened. The moment of approach to the NW, pay attention to the nearby nanowires, b) the needle touches the wire, a platinum layer is placed on top of the touching point. NWs around rose.

After lifting the nanomanipulator, the NW remained on the surface and did not budge.

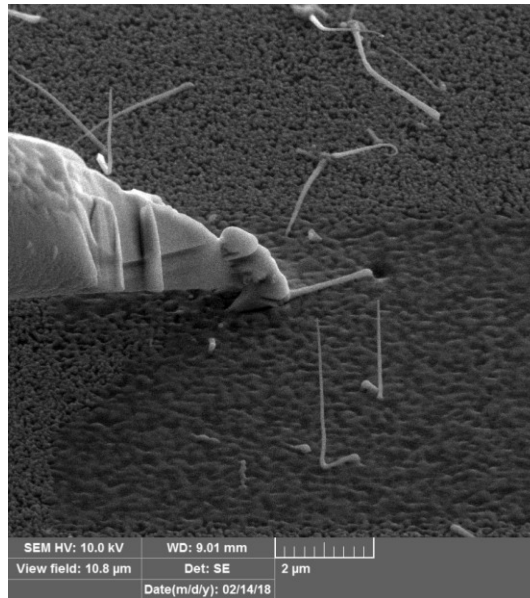

Figure 65. Cut off the end of the NW.

Nanostructures of indium phosphide have an extremely small diameter, therefore they are fragile, and can also be exposed to external effects, as seen from the experiment. However, the GaP NWs investigated in this work have several times larger diameter, comparable to the size of the nanomanipulator. This fact makes it possible to assume that the experiment in the case of GaP will be successful.

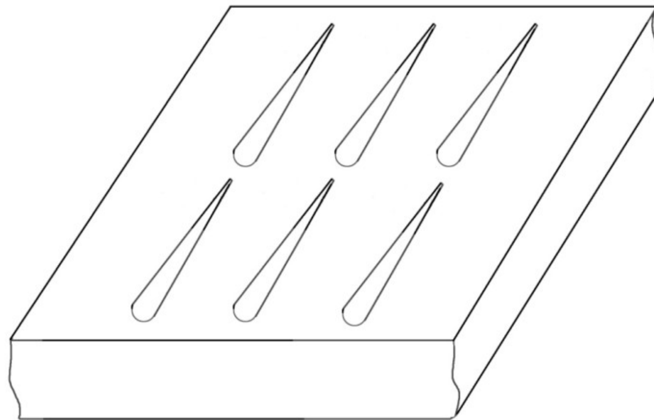

Figure 66. Ideal sample to measure mechanical characteristics of NWs.

Figure 66 shows how an ideal substrate with NWs grown on it for measurement on an AFM could look. The NWs should be strictly oriented in one direction and stand apart from each other at equal distance.

CONCLUSIONS

1) GaP NWs with length L = 1-1.5 μm and D = 50-140 nm exhibit luminescence in the range 1.4-2.6 eV, which indicates the presence of a wurtzite phase.

2) The finding of a specific individual standing inclined NW on the substrate occurs with the combination of optical microscopy and SEM methods. When these two methods are combined, it is possible to manipulate a certain NW, determining its position on the substrate with high accuracy.

3) To work with the tapered thick GaP NWs, it is best to choose stiff, blunt probes for greater NWs bending. The greater the bending, the easier it is to perform subsequent calculations.

4) AFM scanning is best done at tip velocities not exceeding 1 μm/s. If the speed is greater there is a chance to damage the NWs and destroy the structure. If the speed is less, the scan time will increase significantly. NW should be located in the direction parallel to scanning.

5) The Scan Size, number of Lines and Scan Ratio should be chosen in such a way that the resolution of the pixel does not exceed several nanometers. For example, for NWs with a diameter of 50 nm, scan with pixel size of 10 nm will increase error value.

6) Modified probes with a geometry presumably allowing measurements with greater accuracy were proposed and acquired. In particular: use modified probes for better bending of NWs, as well as carry out measurements in various experiment geometries. In addition, another theoretical model, the Timoshenko beam theory, can be used for calculations.

7) The experiment can be performed in various geometries. The more number of geometries will be measured, the more data will be for comparison, and the result will be more accurate.

8) The bending value of the NW at free end with the use of MESP-RC probes reaches up to 80 nm, when a force of 40 nN is applied.

9) The flexibility coefficient of the NW at free end reaches to 2-2.5 m/N, when a force of 40 nN is applied.

10) The scatter of the Young's modulus value occurs due to the uncertainty of the diameter in the model. The parameters to be determined depend very much on the D_{mid}, and in combination with the uncertainty of other parameters it is only possible to estimate the value of the Young's modulus and it is approximately equal E=114.6 GPa when D_{mid} = 65 nm.

11) The greatest error in the calculation occurs due to the definition of D_{mid} of NW. This error can be reduced using either a SEM with a higher resolution, or with the help of AFM. To measure the diameter using the AFM, it is necessary to break off the NW from the substrate and measure its height in the reclining position. However, AFM method has its drawbacks, since it is destructive for the structure.

SUMMARY

The Young's modulus of tapered mixed phase (wurtzite and zincblende) GaP NWs grown on p-Si (111) substrate was measured with AFM QNM bending. All measurements were conducted using a Bruker Multimode 8 microscope in PeakForce QNM mode. The presence of luminescence in a measured sample was experimentally confirmed before measurements.

The main highlights of this work are as follows:

1) The flexibility coefficient of the NW at free end reaches to 2-2.5 m/N, when a force of 40 nN is applied.

2) The parameters to be determined depend very much on the D_{mid}, and in combination with the uncertainty of other parameters it is only possible to estimate the value of the Young's modulus and it is approximately equal E=114.6 GPa when D_{mid} = 65 nm.

3) Modified probes with a geometry presumably allowing measurements with greater accuracy were proposed and acquired.

Moreover, it was found from the literature that GaP NWs can be used for production of photoelectrochemical hydrogen from water and solar energy. This type of fuel is considered as a promising, clean and sustainable type of fuel of the future. The creation and development of renewable energy sources is one of the main directions in the development strategy of the Lappeenranta University of Technology.

The following prospects for the future experiment can be distinguished:

1) Conduct similar experiment on NWs bending using modified probes.

2) Carry out experiment with NWs bending in the various geometries of the experiment.

3) Initially, work with certain NWs, whose diameter is measured with great accuracy.

4) Use Timoshenko beam theory for the calculations.

REFERENCE LIST

[1] Rizal, U., Swain, B. P., & Swain, B. S. (2016, January). Gallium phosphide nanowires for optoelectronic devices. In Microelectronics, Computing and Communications (MicroCom), 2016 International Conference on (pp. 1-4). IEEE.

[2] Lin, H. M., Chen, Y. L., Yang, J., Liu, Y. C., Yin, K. M., Kai, J. J., ... & Chen, C. C. (2003). Synthesis and characterization of core− shell GaP@ GaN and GaN@ GaP nanowires. Nano Letters, 3(4), 537-541.

[3] Traviss, D. J., Schmidt, M. K., Aizpurua, J., & Muskens, O. L. (2015). Antenna resonances in low aspect ratio semiconductor nanowires. Optics express, 23(17), 22771-22787.

[4] Suyatin, D. B., Hällström, W., Samuelson, L., Montelius, L., Prinz, C. N., & Kanje, M. (2009). Gallium phosphide nanowire arrays and their possible application in cellular force investigations. Journal of Vacuum Science & Technology B: Microelectronics and Nanometer Structures Processing, Measurement, and Phenomena, 27(6), 3092-3094.

[5] Hällström, W., Mårtensson, T., Prinz, C., Gustavsson, P., Montelius, L., Samuelson, L., & Kanje, M. (2007). Gallium phosphide nanowires as a substrate for cultured neurons. Nano letters, 7(10), 2960-2965.

[6] Piret, G., Perez, M. T., & Prinz, C. N. (2013). Neurite outgrowth and synaptophysin expression of postnatal CNS neurons on GaP nanowire arrays in long-term retinal cell culture. Biomaterials, 34(4), 875-887.

[7] Prinz, C., Hällström, W., Mårtensson, T., Samuelson, L., Montelius, L., & Kanje, M. (2008). Axonal guidance on patterned free-standing nanowire surfaces. Nanotechnology, 19(34), 345101.

[8] Hasenöhrl, S., Eliáš, P., Šoltýs, J., Stoklas, R., Dujavová-Laurenčíková, A., & Novák, J. (2013). Zinc-doped gallium phosphide nanowires for photovoltaic structures. Applied Surface Science, 269, 72-76.

[9] Standing, A., Assali, S., Gao, L., Verheijen, M. A., Van Dam, D., Cui, Y., ... & Bakkers, E. P. (2015). Efficient water reduction with gallium phosphide nanowires. Nature communications, 6, 7824.

[10] 24. Li, X. F., Zhang, H., & Lee, K. Y. (2014). Dependence of Young′ s modulus of nanowires on surface effect. International Journal of Mechanical Sciences, 81, 120-125.

[11] Fan, S., Bi, S., Li, Q., Guo, Q., Liu, J., Ouyang, Z., ... & Song, J. (2018). Size-dependent Young's modulus in ZnO nanowires with strong surface atomic bonds. Nanotechnology.

[12] Gu, F., Zhang, J., Li, M., Liu, L., & Su, J. (2015). Influence of Defects on the Young's Modulus of [110] Silicon Nanowires with Different Cross Sections. Key Engineering Materials.

[13] Lu, L. B., Yu, H., & Zhang, W. W. (2009, August). Size-dependent and orientation-dependent Young's modulus of silicon nanowires. In ICEM 2008: International Conference on Experimental Mechanics 2008 (Vol. 7375, p. 73753E). International Society for Optics and Photonics.

[14] Welker, H., & Weiss, H. (1956). Group III-Group V Compounds. In Solid State Physics (Vol. 3, pp. 1-78). Academic Press.

[15] Zipperian, T. E., Chaffin, R. J., & Dawson, L. R. (1982). Recent advances in gallium phosphide junction devices for high-temperature electronic applications. IEEE Transactions on Industrial Electronics, (2), 129-136.

[16] Fedorov, P.I., Mohosoev, M.V., & Alekseev, F.P. (1977). Chemistry of gallium, indium and thallium. (In russian Федоров, П. И., Мохосоев, М. В., & Алексеев, Ф. П. (1977). Химия галлия, индия и таллия.)

[17] Semiconductor Wafer, Inc. (SWI) website [accessed at 15.05.2018] Available at http://www.semiwafer.com/gap%20wafer.html

[18] P. B. Johnson and R. W. Christy. Optical constants of the noble metals, Phys. Rev. B 6, 4370-4379 (1972).

[19] Xia, Y., Yang, P., Sun, Y., Wu, Y., Mayers, B., Gates, B., ... & Yan, H. (2003). One-dimensional nanostructures: synthesis, characterization, and applications. Advanced materials, 15(5), 353-389.

[20] Assali, S., Zardo, I., Plissard, S., Kriegner, D., Verheijen, M. A., Bauer, G., ... & Bakkers, E. P. A. M. (2013). Direct band gap wurtzite gallium phosphide nanowires. Nano letters, 13(4), 1559-1563.

[21] Al-Zahrani, H. Y., Pal, J., Migliorato, M. A., Tse, G., & Yu, D. (2015). Piezoelectric field enhancement in III–V core–shell nanowires. Nano Energy, 14, 382-391.

[22] Rizal, U., Swain, B. P., & Swain, B. S. (2016, January). Gallium phosphide nanowires for optoelectronic devices. In Microelectronics, Computing and Communications (MicroCom), 2016 International Conference on (pp. 1-4). IEEE.

[23] Lin, H. M., Chen, Y. L., Yang, J., Liu, Y. C., Yin, K. M., Kai, J. J., ... & Chen, C. C. (2003). Synthesis and characterization of core− shell GaP@ GaN and GaN@ GaP nanowires. Nano Letters, 3(4), 537-541.

[24] Traviss, D. J., Schmidt, M. K., Aizpurua, J., & Muskens, O. L. (2015). Antenna resonances in low aspect ratio semiconductor nanowires. Optics express, 23(17), 22771-22787.

[25] M. D. Birowosuto, G. Zhang, K. Tateno, E. Kuramochi, H. Taniyama, M. Takiguchi, and M. Notomi. Movable high-q nanoresonators realized by semiconductor nanowires on a si photonic crystal platform. Nat. Mater.13, 279–285 (2014).

[26] A. Mirzaei, and A. Miroshnichenko. Electric and magnetic hotspots in dielectric nanowire dimmers. Nanoscale7, 5963–5968 (2015).

[27] S.-K. Kim, R. W. Day, J. F. Cahoon, T. J. Kempa, K.-D. Song, H.-G. Park, and C. M. Lieber. Tuning light absorption in core/Shell silicon nanowire photovoltaic devices through morphological design. Nano Lett.12,4971–4976 (2012).

[28] I.Friedler, C. Sauvan, J. P. Hugonin, P. Lalanne, J. Claudon, and J. M. G´erard. Solid-state single photon sources: the nanowire antenna. Opt. Express 17, 2095–2110 (2009).

[29] R. Paniagua-Dom´ınguez, G. Grzela, J. G. Rivas, and J. A. S´anchez-Gil. Enhanced and directional emission of semiconductor nanowires tailored through leaky/guided modes. Nanoscale 5, 10582–10590 (2013).

[30] Traviss, D. J., Schmidt, M. K., Aizpurua, J., & Muskens, O. L. (2015). Antenna resonances in low aspect ratio semiconductor nanowires. Optics express, 23(17), 22771-22787.

[31] Malizia, M., Seger, B., Chorkendorff, I., & Vesborg, P. C. (2014). Formation of ap–n heterojunction on GaP photocathodes for H 2 production providing an open-circuit voltage of 710 mV. Journal of Materials Chemistry A, 2(19), 6847-6853.

[32] Liu, C., Sun, J., Tang, J., & Yang, P. (2012). Zn-doped p-type gallium phosphide nanowire photocathodes from a surfactant-free solution synthesis. Nano letters, 12(10), 5407-5411.

[33] Hu, S., Shaner, M. R., Beardslee, J. A., Lichterman, M., Brunschwig, B. S., & Lewis, N. S. (2014). Amorphous TiO2 coatings stabilize Si, GaAs, and GaP photoanodes for efficient water oxidation. Science, 344(6187), 1005-1009.

[34] Lieber, C. M., & Wang, Z. L. (2007). Functional nanowires. MRS bulletin, 32(2), 99-108.

[35] Chen, L., Lu, W., & Lieber, C. M. (2014). Semiconductor nanowire growth and integration. In Semiconductor Nanowires (pp. 1-53).

[36] Lukashin, AV, Eliseev, AA, & Pomerantseva, EA (2007). Functional properties of one-dimensional systems. Moscow: Moscow State University. (In Russian: Лукашин, А. В., Елисеев, А. А., & Померанцева, Е. А. (2007). Функциональные свойства одномерных систем. Москва: МГУ.)

[37] A.W. Vere, Crystal Growth: Principles and Progress, Plenum, New York, 1987.

[38] Wagner, R. S., & Ellis, W. C. (1964). Vapor‐liquid‐solid mechanism of single crystal growth. Applied Physics Letters, 4(5), 89-90.

[39] V. Schmidt, J. V. Wittemann and U. G¨osele, Growth, Thermodynamics, and Electrical Properties of Silicon Nanowires, Chem. Rev., 2010, 110(1), 361–388.

[40] Castro, T., Reifenberger, R., Choi, E., & Andres, R. P. (1990). Size-dependent melting temperature of individual nanometer-sized metallic clusters. Physical review B, 42(13), 8548.

[41] Givargizov, E. I. (1993). Ultrasharp tips for field emission applications prepared by the vapor–liquid–solid growth technique. Journal of Vacuum Science & Technology B: Microelectronics and Nanometer Structures Processing, Measurement, and Phenomena, 11(2), 449-453.

[42] Gudiksen, M. S., Wang, J., & Lieber, C. M. (2001). Synthetic control of the diameter and length of single crystal semiconductor nanowires. The Journal of Physical Chemistry B, 105(19), 4062-4064.

[43] Berdichevsky, Y., & Lo, Y. H. (2005). Fabrication and evaluation of conducting polymer nanowire heterostructures. MRS Online Proceedings Library Archive, 872.

[44] del Valle, M. A., Ramos, A. C., Diaz, F. R., & Gacitua, M. A. (2015). Electrosynthesis and Characterisation of Polymer Nanowires from Thiophene and its Oligomers. Journal of the Brazilian Chemical Society, 26(11), 2313-2320.

[45] Graves, J. E., Bowker, M. E. A., Summer, A., Greenwood, A., de León, C. P., & Walsh, F. C. (2017). A new procedure for the template synthesis of metal nanowires. Electrochemistry Communications.

[46] Şişman, İ. (2011). Template-assisted electrochemical synthesis of semiconductor nanowires. Nanowires–Implementations and Applications, 41-58.

[47] Hsu, Y. K., Yu, C. H., Lin, H. H., Chen, Y. C., & Lin, Y. G. (2013). Template synthesis of copper oxide nanowires for photoelectrochemical hydrogen generation. Journal of Electroanalytical Chemistry, 704, 19-23.

[48] Furneaux, R. C., Rigby, W. R., & Davidson, A. P. (1989). The formation of controlled-porosity membranes from anodically oxidized aluminium. Nature, 337(6203), 147.

[49] Fleischer, R. L., Price, P. B., & Walker, R. M. (1975). Nuclear tracks in solids: principles and applications. Univ of California Press.

[50] Tonucci, R. J., Justus, B. L., Campillo, A. J., & Ford, C. E. (1992). Nanochannel array glass. Science, 258(5083), 783-785.

[51] Wu, C. G., & Bein, T. (1994). Conducting polyaniline filaments in a mesoporous channel host. Science, 264(5166), 1757-1759.

[52] Fan, S., Chapline, M. G., Franklin, N. R., Tombler, T. W., Cassell, A. M., & Dai, H. (1999). Self-oriented regular arrays of carbon nanotubes and their field emission properties. Science, 283(5401), 512-514.

[53] Ajayan, P. M., Stephan, O. B. A. U. D. P., Redlich, P., & Colliex, C. (1995). Carbon nanotubes as removable templates for metal oxide nanocomposites and nanostructures. Nature, 375(6532), 564.

[54] Kawamura, G., Muto, H., & Matsuda, A. (2014). Hard template synthesis of metal nanowires. Frontiers in chemistry, 2, 104.

[55] Thomas, G. (1999). The impact of electron microscopy on materials research. In Impact of Electron and Scanning Probe Microscopy on Materials Research (pp. 1-24). Springer, Dordrecht.

[56] Mohale, G. T. M., Beukes, J. P., Kleynhans, E. L. J., Van Zyl, P. G., Bunt, J. R., Tiedt, L. R., ... & Jordaan, A. (2017). SEM image processing as an alternative method to determine chromite pre-reduction. Journal of the Southern African Institute of Mining and Metallurgy, 117(11), 1045-1052.

[57] Webb, R. I., & Schieber, N. L. (2018). Volume Scanning Electron Microscopy: Serial Block-Face Scanning Electron Microscopy Focussed Ion Beam Scanning Electron Microscopy. In Cellular Imaging (pp. 117-148). Springer, Cham.

[58] Goldstein, J. I., Newbury, D. E., Michael, J. R., Ritchie, N. W., Scott, J. H. J., & Joy, D. C. (2017). Scanning electron microscopy and X-ray microanalysis. Springer.

[59] Moshnikov V.A., & Spivak Yu.M. (2009). Atomic force microscopy for nanotechnology and analysis: Textbook. SPb ETU LETI Publishing house, 80, 12. (In Russian: Мошников, В. А., & Спивак, Ю. М. (2009). Атомно-силовая микроскопия для нанотехнологии и диагностики: Учеб. пособие. СПб.: Изд-во СПбГЭТУ «ЛЭТИ, 80, 12.)

[60] V.Mironov, Fundamentals of Scanning Probe Microscopy, N.Novgorod, 2004 (in Russian).

[61] Kopycinska-Müller, M., Geiss, R. H., & Hurley, D. C. (2006). Contact mechanics and tip shape in AFM-based nanomechanical measurements. Ultramicroscopy, 106(6), 466-474.

[62] Giessibl, F. J. (2005). AFM's path to atomic resolution. Materials Today, 8(5), 32-41.

[63] Howland, R., Benatar, L., & Instruments, P. S. (1996). A practical guide to scanning probe microscopy. Park scientific instruments.

[64] Dimension FastScan User Guide [accessed at 15.05.2018] Available at http://www.nanophys.kth.se/nanophys/facilities/nfl/afm/fast-scan/bruker-help/DIcon_webhelp.htm

[65] Magonov, S., Surtchev, M., Belikov, S., Malovichko, I., & Leesment, S. (2015). Quantitative nanomechanical measurements in Hybrid mode atomic force microscopy. NT-MDT Application note, 90.

[66] Dunaevskiy, M., Geydt, P., Lähderanta, E., Alekseev, P., Haggrén, T., Kakko, J. P., ... & Lipsanen, H. (2017). Young's Modulus of Wurtzite and Zinc Blende InP Nanowires. Nano letters, 17(6), 3441-3446.

[67] Lucas, M., Leach, A. M., McDowell, M. T., Hunyadi, S. E., Gall, K., Murphy, C. J., & Riedo, E. (2008). Plastic deformation of pentagonal silver nanowires: comparison between AFM nanoindentation and atomistic simulations. Physical Review B, 77(24), 245420.

[68] Khalil, A., Singh Lalia, B., Hashaikeh, R., & Khraisheh, M. (2013). Electrospun metallic nanowires: Synthesis, characterization, and applications. Journal of Applied Physics, 114(17), 12_1.

[69] Shanmugham, S., Jeong, J., Alkhateeb, A., & Aston, D. E. (2005). Polymer nanowire elastic moduli measured with digital pulsed force mode AFM. Langmuir, 21(22), 10214-10218.

[70] Ерофеев, В. И., Кажаев, В. В., Лисенкова, Е. Е., & Семерикова, Н. П. (2011). Динамическое поведение балок моделей Бернулли-Эйлера, Рэлея и Тимошенко, лежащих на упругом основании (сравнительный анализ). Вестник Нижегородского университета им. НИ Лобачевского, (5-3). (Erofeev, V.I., Kazhaev, V.V., Lisenkova, E.E., & Semerikova, N.P. (2011) Dynamic behavior of the beams of Bernoulli-Euler, Rayleigh, and Timoshenko models lying on an elastic foundation (comparative analysis). Bulletin of the Nizhny Novgorod University of N.I. Lobachevsky, (5-3)) (In Russian)

[71] Geydt, P., Dunaevskiy, M. S., & Lähderanta, E. (2017). Opportunities of Scanning Probe Microscopy for Electrical, Mechanical and Electromechanical Research of Semiconductor Nanowires. In Nanowires-New Insights. InTech.

[72] Gere, J. M., & Timoshenko, S. P. (1984). Mechanics of materials.

[73] Dhaka, V., Pale, V., Khayrudinov, V., Kakko, J. P., Haggren, T., Jiang, H., ... & Lipsanen, H. (2016). Synthesis and properties of ultra-long InP nanowires on glass. Nanotechnology, 27(50), 505606.

[74] Haggren, T., Khayrudinov, V., Dhaka, V., Jiang, H., Shah, A., Kim, M., & Lipsanen, H. (2018). III–V nanowires on black silicon and low-temperature growth of self-catalyzed rectangular InAs NWs. Scientific reports, 8(1), 6410.

[75] Roest, A. L., Verheijen, M. A., Wunnicke, O., Serafin, S., Wondergem, H., & Bakkers, E. P. (2006). Position-controlled epitaxial III–V nanowires on silicon. Nanotechnology, 17(11), S271.

[76] Hocevar, M., Conesa-Boj, S., & Bakkers, E. (2015). Hybrid III–V/Silicon Nanowires. In Semiconductors and Semimetals (Vol. 93, pp. 231-248). Elsevier.

[77] Wang, S. Q., & Ye, H. Q. (2003). First-principles study on elastic properties and phase stability of III–V compounds. physica status solidi (b), 240(1), 45-54.

[78] Martin, R. M. (1972). Relation between elastic tensors of wurtzite and zinc-blende structure materials. Physical Review B, 6(12), 4546.

Appendix I. List of Figures

Figure 1. Crystal structure: a) zincblende; b) wurtzite (white – P, yellow – Ga).

Figure 2. GaP Wafers grown by Czochralski extrusion taken from [17].

Figure 3. a)SEM image of GaP NWs (white) located on a flat Si substrate (grey background), b) TEM image of NW showing mixed ZB/WZ phases, scale bar: 20 nm.[35].

Figure 4. Nanowire FET source–drain current I_{SD} versus source–drain voltage V_{SD} characteristics measured at variable gate voltage V_G taken from [8].

Figure 5. SEM-images showing: a) ordered array of GaP NWs, b) nerve cells from dissociated dorsal root ganglia on a GaP NW array, c) retinal cells on GaP NWs, d) axons grow in the middle of two rows of NWs. The images are taken from [4-7].

Figure 6. Linear sweep voltammograms for direct comparison of NW (red) and planar (black) samples with molybdenum sulphide catalyst, performed under chopped 100 $mWcm^{-2}$ AM1.5 illumination, in aqueous solution pH 0 with $HClO_4$ as supporting electrolyte. Also showing open circuit potential (V_{OC}), short circuit current (I_{SC}) and fill factor ff (filled square/empty square) [9].

Figure 7. Schematic representation of the phased growth of a crystal occurring during a heterogeneous reaction taken from [36].

Figure 8. Schematic representation of the main stages of crystal growth using the Vapor-Liquid-Solid Mechanism: (a) initial nucleation and (b) continued growth taken from [36].

Figure 9. A diagram illustrating a general idea of the diameter and length control of NWs by varying the size of the catalyst droplet and the growth time, respectively [42].

Figure 10. SEM images: a) Template from anodic aluminum oxide filled with cobalt, b) An array of cobalt NWs obtained by the method of template synthesis taken from [54].

Figure 11. Basic construction of a SEM taken from [58].

Figure 12. Areas of signals, when the surface of the sample is irradiated with an electron beam.

Figure 13. Dependence of the interaction force on the distance between the needle and the surface of the sample. "0" is the boundary of the contact mode in the AFM [59].

Figure 14. Image of cantilever and tip: 1 is the rectangular base (substrate); 2 is the A-shaped cantilever; 3 is a pyramidal probe (tip).

Figure 15. Schematic diagram of the AFM scanning unit with registration of cantilever deflection by reflected laser beam deflection taken from [59].

Figure 16. Schematic representation of a sensor and a scheme for optical recording of cantilever bending; 1 ... 4 are photodiode section numbers [59].

Figure 17. The correspondence between the type of flexural deformations of the cantilever and the change in the position of the spot on the photodiode [59].

Figure 18. Different types of AFM probes: a) pyramidal, b) cone-shaped [59].

Figure 19. The definition of lateral resolution by the Rayleigh criterion [63].

Figure 20. Comparison of the real image with the image in the presence of tip convolution [63].

Figure 21. Peak Force QNM Specification given by Bruker Company [65].

Figure 22. Force-versus-time, Fvt (left), and force-versus-distance, FvZ (right), curves in an oscillatory cycle of the QNM [65].

Figure 23. Different experiment geometries.

Figure 24. Deformation of a Timoshenko beam (blue) compared with that of an Euler-Bernoulli beam (red).

Figure 25. Photoluminescence spectra of GaP NWs obtained with different technological conditions.

Figure 26. SEM images of GaP NWs: a) sample 254, b) sample 262.

Figure 27. SEM images of GaP NWs: a) location on the substrate, b) individually standing NW, conical shape is visualized.

Figure 28. a) AFM probe holder with installed probe; b) In progress.

Figure 29. Modulus ranges covered by various probes. The modulus of the reference sample for each range is indicated as well.

Figure 30. Optical microscopy window: a) no probe installed, b) the probe is out of focus, the probe on a considerable distance from the sample's surface, c) the probe is almost in focus, the probe is at a small distance from the sample surface.

Figure 31. Placement of AFM knobs.

Figure 32. a) The parameters given in the user's manual, b) the real window in the working software.

Figure 33. Deflection vs. Z plot.

Figure 34. The Set Realtime Channel Sensitivities window.

Figure 35. The Force Monitor window.

Figure 36. The Set Sensitivity window.

Figure 37. Select Thermal Tune Frequency Range.

Figure 38. The Thermal Tune panel.

Figure 39. SEM images of the sample.

Figure 40. Window of the optical microscope of the AFM system opened in the software. To the left, for convenience, sample image is open.

Figure 41. NanoScope program window contains data for channels Height (in Trace and Retrace), Deformation and PeakForce.

Figure 42. Comparison of the data obtained by AFM and SEM, scale bar: 5 μm.

Figure 43. The first parameters to be changed at the beginning of the measurements.

Figure 44. Scanning parameters and AFM image scan of 20 microns.

Figure 45. Single NW scanning on process, left is Height channel, right is PeakForce channel.

Figure 46. Single NW scanning on process, the angle of scanning was changed, left is Height channel, right is PeakForce channel.

Figure 47. Obtaining the height profile of a NW in the NanoScope Analysis 1.8 program, channel Height.

Figure 48. Obtaining the deformation profile of a NW in the NanoScope Analysis 1.8 program, channel Deformation.

Figure 49. Obtaining the force profile of a NW in the NanoScope Analysis 1.8 program, channel PeakForce.

Figure 50. The threefold symmetry of wires grown in the [111] direction on a (111) surface can be clearly seen. Wires grown perpendicular to the (111) surface can be seen as dots. (a) A schematic top view and (b) a side view to illustrate the four [111] directions in which the wires grow [75-76].

Figure 51. The height profiles of the NW obtained with different peak forces.

Figure 52. The height profiles of the NW obtained with different peak forces, the profile is selected along the length of the NW.

Figure 53. Bending profiles for various values of peak force.

Figure 54. Flexibility profiles for various values of peak force.

Figure 55. Flexibility profile of NW, averaged curve.

Figure 56. Flexibility profile of NW, averaged curve (black) and Fitting curve (Red): a) D_{mid}=60 nm; b) D_{mid}=65 nm; c) D_{mid}=70 nm; d) D_{mid}=90 nm.

Figure 57. The variation of Young's modulus value, arising in this theoretical model due to the impossibility of accurate determination of the D_{mid}.

Figure 58. The way of NW investigation by means of AFM.

Figure 59. The way of NW investigation by means of AFM with modified cantilever.

Figure 60. Schematic front view of cantilevers. Desirable shape of the tip.

Figure 61. The way of the probe etching via FIB.

Figure 62. Front view of modified cantilevers a) Bruker Scanasyst AIR, b) Bruker Scanasyst PIT.

Figure 63. Double-bonded NW structure.

Figure 64. a) The needle of the nanomanipulator (on the left) is already sharpened. The moment of approach to the NW, pay attention to the nearby nanowires, b) the needle touches the wire, a platinum layer is placed on top of the touching point. NWs around rose.

Figure 65. Cut off the end of the NW.

Figure 66. Ideal sample to measure mechanical characteristics of NWs.